journal of the mechanical behavior of biomedical materials 131 (2022) 105246

Contents lists available at ScienceDirect

Journal of the Mechanical Behavior of Biomedical Materials

journal homepage: www.elsevier.com/locate/jmbbm

Multi-material cellular structured orthopedic implants design: In vitro and bio-tribological performance

M.M. Costa [a,b,*], R. Lima [c,d], N. Alves [e], N.A. Silva [c,d], M. Gasik [f,g], F.S. Silva [a,b], F. Bartolomeu [a,b,1], G. Miranda [h,i,1]

[a] *Center for MicroElectroMechanical Systems (CMEMS-UMinho), University of Minho, Campus de Azurém, 4800-058, Guimarães, Portugal*
[b] *LABBELS –Associate Laboratory, Braga/Guimarães, Portugal*
[c] *Life and Health Sciences Research Institute (ICVS), School of Medicine, University of Minho, Campus de Gualtar, 4710-057, Braga, Portugal*
[d] *ICVS/3B's - PT Government Associate Laboratory, Braga/Guimarães, Portugal*
[e] *Centre for Rapid and Sustainable Product Development Polytechnic Institute of Leiria, Rua General Norton de Matos, Apartado 4133, 2411-901, Leiria, Portugal*
[f] *School of Chemical Engineering, Aalto University Foundation, FI-00076, Espoo, Finland*
[g] *Seqvera Ltd., Helsinki, Finland*
[h] *CICECO, Aveiro Institute of Materials, University of Aveiro, 3810-193, Aveiro, Portugal*
[i] *Department of Materials and Ceramic Engineering, University of Aveiro, 3810-193, Aveiro, Portugal*

ARTICLE INFO

Keywords:
Multi-material structures
NiTi-Based
Ti6Al4V-based
In vitro
Bio-tribological experiments

ABSTRACT

In this study, Selective Laser Melting (SLM) was used to produce mono-material Ti64Al4V- and NiTi-cubic cellular structures with an open-cell size and wall thickness of 500 μm and 100 μm, respectively. Bioactive beta-tricalcium phosphate (βTCP) and polymer poly-ether-ether ketone (PEEK) were used to fill the produced structures open-cells, thus creating multi-material components. These structures were characterized *in vitro* in terms of cell viability, adhesion, differentiation and mineralization. Also, bio-tribological experiments were performed against bovine plate to mimic the moment of implant insertion. Results revealed that metabolic activity and mineralization were improved on SLM mono-material groups, when compared to the control group. All cell metrics were improved with the addition of PEEK, conversely to βTCP where no significant differences were found. These results suggest that the proposed solutions can be used to improve implants performance.

1. Introduction

Nowadays hip implants are dense metallic components that replace an injured joint to recover joint functionality and pain-free mobility (Costa et al., 2019c; Wedemeyer et al., 2019). However, hip implants have limited lifespan, especially in younger active patients, and revision surgeries, usually more expensive and painful, are inevitable (Bartolomeu et al., 2020a; Costa et al., 2019c; Mitra et al., 2021).

This is related with loss of fixation between the implant and bone (Bartolomeu et al., 2020a; Costa et al., 2021), since commercially available solutions are markedly different from natural bone in a mechanical and biomechanical points of view. There is a stiffness mismatch between the existing implant metallic materials and bone, leading to a stress shielding effect, where there is a deficient stress distribution to the surrounding bone, resulting in bone resorption, implant loosening and consequent failure (Alabort et al., 2019; Bartolomeu et al., 2020a, 2020b; Chen et al., 2017; Shekhawat et al., 2021; Solanke et al., 2021). Besides, a non-uniform contact pressure between implant and bone can also lead to the same outcome (Bartolomeu et al., 2020a, 2020b). Lastly, implant micro-motions together with a poor wear resistance of implant materials can lead to wear particles release to the surrounding bone, causing inflammatory reactions and peri-prosthetic osteolysis (bone degeneration) (Bartolomeu et al., 2020a, 2020b; Shekhawat et al., 2021; Solanke et al., 2021).

To overcome these problems, adding controlled porosity to the implant will allow implant stiffness tailoring to values closer to that of bone (Alabort et al., 2019). Ti6Al4V (Ti64) is the most widely used material in implantology due to its mechanical strength, high biocompatibility and corrosion resistance, although still having high elastic modulus when compared to cortical bone (Bartolomeu et al., 2019c,

---

[*] Corresponding author. Center for MicroElectroMechanical Systems (CMEMS-UMinho), University of Minho, Campus de Azurém, 4800-058, Guimarães, Portugal.
E-mail address: amafmcosta@gmail.com (M.M. Costa).

[1] Co-last authorship.

https://doi.org/10.1016/j.jmbbm.2022.105246
Received 23 February 2022; Received in revised form 11 April 2022; Accepted 17 April 2022

2020a, 2020b; Costa et al., 2019a, 2019b, 2019c; Faria et al., 2018; Yuan et al., 2019). In this sense, by creating porous implants, it is possible to decrease the modulus of a Ti64 component, and reduce the stress shielding effect (Chen et al., 2017). This controlled porosity can be achieved by manufacturing the implant through Additive Manufacturing techniques, particularly Selective Laser Melting (SLM).

By SLM it is possible to manufacture, in a layer-by-layer process, components with high degree of complexity from CAD data (Bartolomeu et al., 2020a, 2020b; Costa et al., 2019a, 2019b; Parvizi et al., 2021; Yuan et al., 2019). Besides elastic modulus tailoring, this interconnected porosity will also assure nutrients flow and oxygen supply for vascularization and osteogenesis, for cells to adhere and proliferate and allowing bone ingrowth, crucial to enhance bone-implant fixation (mechanical interlocking) (Bartolomeu et al., 2020a; Costa et al., 2019a, 2019b, 2021; Gao et al., 2020; Ran et al., 2018; Yuan et al., 2019). Ran et al. (2018) evaluated the *in vitro* biological performance of different Selective Laser Melted porous Ti6Al4V implants (500, 700 and 900 μm pore sizes), and concluded that scaffolds with lower open-cell sizes were suitable for cell adhesion whilst higher sizes are beneficial for cell proliferation. In a different study, Yang et al. (2017) analyzed *in vitro* response of porous Ti6Al4V implants with different pore sizes fabricated by Laser Beam Melting, concluding that best cellular growth, migration and adhesion was found for both 350 and 500 μm pore size groups. Chen et al. (Z. Y. Chen et al., 2020), reported a similar outcome, revealing that Ti6Al4V structures with 500 μm pore size displayed the greatest cell proliferation, differentiation and bone ingrowth.

Nickel-titanium (NiTi) alloy presents high corrosion resistance, high biocompatibility and two attractive and special properties, shape memory effect and superelasticity (Bartolomeu et al., 2020a, 2020b; Costa et al., 2021; Dulski et al., 2018; Hung et al., 2015; Mwangi et al., 2019; Parvizi et al., 2021; Sevcikova and Pavkova Goldbergova, 2017). When compared to Ti64, NiTi Young's Modulus is lower and its wear resistance is higher, thus reducing the stress shielding effect and wear debris release, respectively. On the other hand, its shape memory effect can also be used to assure a uniform contact pressure between implant and bone (Bartolomeu et al., 2020b; Costa et al., 2021; Mwangi et al., 2019).

The creation of multi-material solutions can be extremely advantageous to fulfill different requirements in distinct regions of a same component, by gathering different properties, not achievable in a single material (Costa et al., 2019c). Poly-ether-ether ketone (PEEK) is a polymeric material with high biocompatible and corrosion resistance, also owning an excellent wear resistance, very attractive to enhance implant wear performance (Costa et al., 2019b, 2021; Verma et al., 2021). Bioactive β-tricalcium phosphate (βTCP) can also provide bioactivity to a metal implant made from Ti6Al4V or NiTi since is very similar to the mineral phase of bone and will interact with the biological environment, inducing a faster osseointegration (Costa et al., 2019a, 2019b, 2019c; Dulski et al., 2018; Mitra et al., 2021). Zheng et al. (2021) evaluated the biocompatibility and mineralization *in vitro* of PEEK scaffolds and PEEK-HA composites manufactured by additive manufacturing and showed that, although both options displayed good cytocompatibility, the addition of hydroxyapatite enhanced cell adhesion and mineralization. Harb et al. (2020) performed PMMA-TiO_2 and PMMA-ZrO_2 coatings, also modified with hydroxyapatite and βTCP, on Ti6Al4V implants and revealed an enhanced ALP activity and calcium concentration on the coatings, being even higher for the coating with the bioactive materials, when compared to Ti6Al4V.

However, both PEEK and βTCP mechanical properties are not suitable for load-bearing applications (Costa et al., 2019a, 2019c; Peñarrieta-Juanito et al., 2018), in this sense, combining them with materials like Ti64 and/or NiTi, will guarantee the necessary biological and mechanical requirements.

In this context, creating multi-material solutions to bring multi-functionality to implants and overcome the current implant problems, aiming to create implants for life, is the main focus of the present study. SLM will be used to manufacture NiTi and Ti64 cellular structures that will be further impregnated either by PEEK or βTCP aiming to meet specific requirements namely: lowering implant elastic properties; promoting bone ingrowth through the interconnected porosity; improve wear resistance by introducing materials as NiTi and PEEK; or add bioactivity through βTCP incorporation. It is extremely important to mention that this type of multi-material approaches, are scarcely discussed in literature for such applications.

Table 1
Group description and fabrication method.

Group	Description	Fabrication Method
G1	Ti64 SLA	Cast SLA-treated
G2	Ti64 SLM	SLM
G3	Ti64-βTCP	SLM+PS
G4	Ti64 -PEEK	SLM+HP
G5	NiTi	SLM
G6	NiTi-βTCP	SLM+PS
G7	NiTi-PEEK	SLM+HP

SLA – Sandblast-acid etching; PS – press and sintering.
HP – hot pressing.

For that purpose, in the following study, different solutions gathering different materials were manufactured and characterized *in vitro* to assess cell viability, adhesion and metabolic activity and its potential differentiation and mineralization as well as their implant-bone tribological performance during implantation.

2. Experimental details

2.1. Specimens fabrication

In the present study, seven different groups were designed and manufactured and further characterized, with details being presented in Table 1.

As a representation of commercially available implants, dense Ti64 cast/forged commercial rod, obtained from *Titanium Products (United Kingdom)*, having 6 mm diameter, was cut and exposed to sandblast-acid etching process (SLA), aiming to display the moderate roughness topography frequently used in implants (between 2 and 4 μm) (Bartolomeu et al., 2019b; Costa et al., 2019c; Straumann, 2011).

These specimens were sandblasted with spherical alumina particles and further acid etched in a 32% HCl, 96% H_2SO_4 and H_2O (2,1,1) solution, for 5 min at 65 °C ± 4 °C being afterwards ultrasonically cleaned in isopropanol for 5 min. This group, schematically represented in Fig. 1 (A), will be named throughout this manuscript as G1.

Ti64 and NiTi were used as raw powdered materials for cellular structures production. Ti64 (ELI – grade 23) starting powder was purchased from *SLM Solutions, Germany (UK81278)*, having a spherical morphology with a particle size diameter (d50) of 46.94 μm, whilst NiTi powder was obtained by atomizing (at *TLS technique GmbH, Germany*) a $Ni_{50.8}Ti_{49.2}$ ingot (at.%) from *SAES Smart Materials (USA)*, using an electrode induction-melting gas atomization (EIGA) technique. The final powder displayed a spherical morphology with a particle size, d50, of 47.5 μm.

NiTi and Ti64 cellular structures were designed and fabricated using an SLM equipment (*SLM Solutions, model 125HL, Germany*) having a 400 W Ytterbium-fiber laser with 87 μm diameter. The process occurred under argon atmosphere, with a heated platform at 200 °C, using the 90 W laser power, 600 mm/s scan speed, 30 μm layer thickness and 90 μm scan spacing. Fig. 1 (B) illustrates the SLM manufacturing process used for Ti64 and NiTi cellular structures. These Ti64 and NiTi cellular structures, CAD designed with an open-cell size of 500 μm and wall thickness of 100 μm, will be used as G2 and G5 groups, respectively, and will also act as base specimens for multi-material production.

Multi-material specimens were produced by impregnating βTCP or PEEK into these cellular structures. For that purpose, βTCP spherical

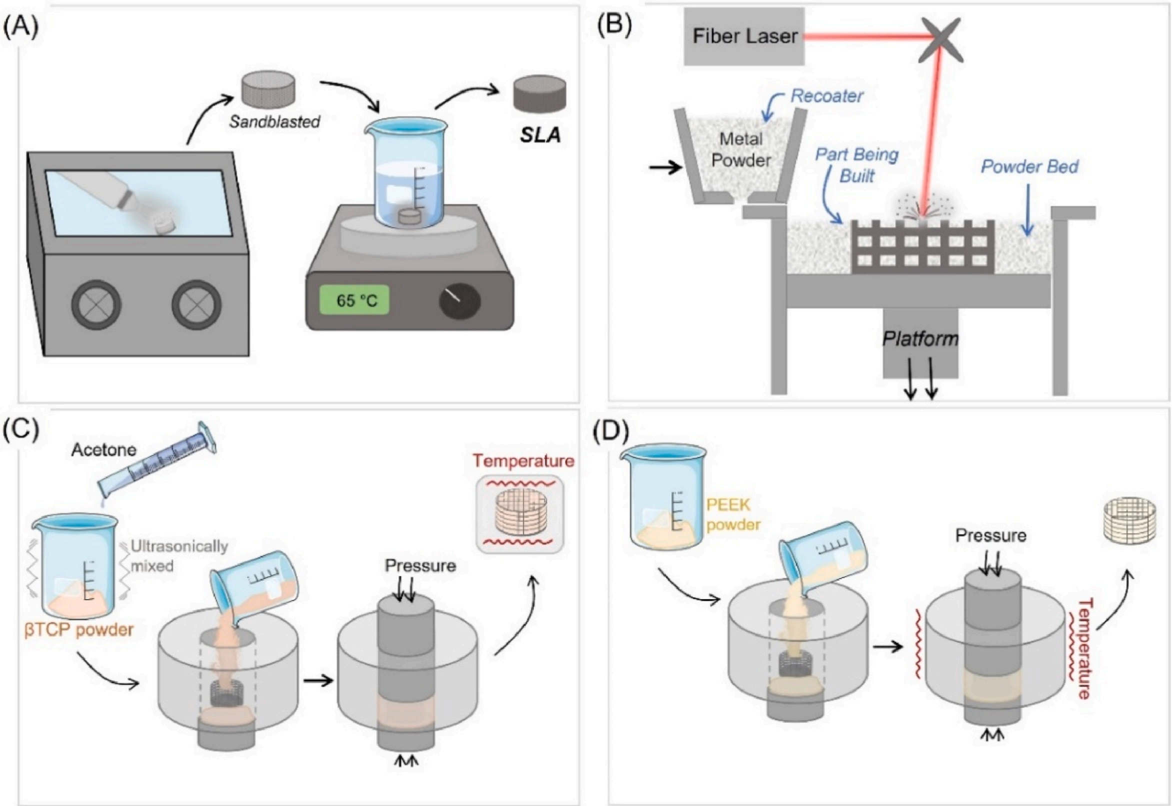

Fig. 1. Schematic representation of the fabrication methods for the produced specimens (A) Sandblast Acid Etching (SLA); (B) SLM; (C) βTCP and (D) PEEK impregnation.

powder with a d50 of 2.26 μm was purchased from *Trans-Tech*, Inc. *(USA)* while PEEK powder (*VESTAKEEP, 2000FP*), d50 of 50 μm, having an irregular shape was obtained from *Evonik Industries (Germany)*.

For multi-material structures with βTCP, the process begins by mixing the bioactive powder with acetone to obtain a viscous solution (≈ 36% (w/v)). This solution and the cellular structures were inserted inside a 10 mm (diameter) steel die and a hydraulic press (*Mega PR50, Spain*) was used, at a pressure of ≈ 74 MPa, for 10 min, to force the entrance of the solution into the structures' open cells. The multi-material specimens were then sintered in a tubular furnace (*Termolab, Portugal*) at 1100 °C for 2 h, at a heating rate of 8 °C/min, in an argon atmosphere for NiTi-βTCP specimens and high vacuum for Ti6Al4V-βTCP specimens.

Regarding multi-material structures with PEEK, hot pressing (HP) technique was used for the structure's impregnation with an in house developed equipment. In this process, PEEK powder and the NiTi or Ti6Al4V cellular structures were inserted inside an 8 mm graphite die, followed by its positioning inside a hot pressing equipment. Under vacuum, a residual pressure was firstly applied to accommodate the polymeric powder, and the temperature was raised up to 380 °C (above PEEK melting point (345 °C)). The induction heating was turned off and when the temperature reaches 300 °C, a pressure of ≈ 10 MPa was applied for approximately 15 s to force the polymer to fill the open cells. After repeating this cycle two times, the specimen was allowed to cool inside the HP equipment, till room temperature. Fig. 1(C) and (D) displays a schematic representation of βTCP and PEEK impregnation process, respectively.

Additionally, a final group of multi-material samples, named throughout the manuscript as bimetallic, were manufactured and will act as a proof-of-concept by introducing a next level of multi-material multi-functionality.

In this context, NiTi–Ti64 bimetallic cellular structures were produced by SLM according to the following steps: a NiTi region was firstly printed, up to a predefined layer number; the fabrication process was stopped and all the excess/loose NiTi powder was removed from the platform and replaced by Ti64 powder, manually; Ti6Al4V region was then printed on top of the previously manufactured NiTi, up to the final layer designed in the CAD model. The processing parameters used were selected according to the ones defined for mono-material production. These samples were CAD designed to have an open cell and wall thickness of 500 μm and 100 μm, respectively. Afterwards, for tri-material production, NiTi–Ti64 specimens' open-cells were filled with PEEK following the same process used for G4 and G7 groups. Similarly, NiTi–Ti64-βTCP specimens were produced as G3 and G6 groups.

Before characterization, all groups were polished with SiC abrasive papers up to P4000, ultrasonically cleaned with isopropanol, dried in vacuum for 30 min and stored in a desiccator until characterization.

2.2. Morphological and crystallographic characterization

Surface morphology of the specimens from the different groups was observed by Scanning Electron Microscopy (SEM), before the experiments and after bio-tribological tests, using a *JSM.*6010LV equipment from *JEOL (Japan)*. Moreover, X-ray diffraction analysis (XRD) was also performed on the produced specimens, before characterization, using a *Bruker AXS D8 Discover (USA)* equipment from 10 to 90°, with a step size and counting time of 0.02° and 1s, respectively. Energy-dispersive X-Ray spectroscopy analysis (EDS) was also made (*Oxford Instruments Inc, X-act, United Kingdom*), when needed, after bio-tribological tests in specific sites of the specimens.

2.3. *In vitro experiments*

2.3.1. *Cytotoxicity assessment*

The short-term cytotoxicity of the produced scaffolds was performed according to Silva et al. (2010), in triplicate. The scaffolds were placed in minimum essential medium (MEM) and extracted after 24 h, 7 and 28 days. In all tests, material weight-to-extract fluid rate was constant (0.2 g ml^{-1}) and after each timepoint the extracts were filtered using a 0.45 mm pore-size filter.

2.3.1.1. Cell culture. Rat lung fibroblasts-L929 cell line from *European Collection of Cell Cultures* were seeded in a 24-well plate (n = 3, 5 × 10^3 cells well^{-1}) and then cultured at 37 °C in a humidified atmosphere with 5% CO_2, for 24 h in Dulbecco's modified Eagle's medium, DMEM (*Sigma, Missouri, USA*). This media was supplemented with 10% fetal bovine serum (FBS) (*Gibco, Barcelona, Spain*) and 1% antibiotic-antimycotic mixture (*Sigma*).

2.3.1.2. MEM extraction test. Twenty-four hours after cell seeding, the culture medium was removed from the wells and replaced by the MEM extraction fluid. The L929 cultures were then incubated for 72 h at 37 °C in a humidified atmosphere with 5% CO_2. Live cells were stained with calcein-AM (1 mg ml^{-1}; *Molecular Probes, Eugene, OR*) and nonviable cells with propidium iodide (0.1 mg ml^{-1}; *Molecular Probes*). After incubation for 15 min at 37 °C in a humidified atmosphere with 5% CO_2, cultures were observed under a fluorescence microscope (*BX-61; Olympus, Hamburg, Germany*). Latex extracts were used as negative controls for cell survival, whereas standard culture medium was used as positive control.

2.3.2. *Dynamic direct contact assay*

Cell attachment and proliferation can be assessed by direct contact assay in order to evaluate the *in vitro* biocompatibility of the scaffolds (Ribeiro-Samy et al., 2013). Human Mesenchymal Stem Cells (hMSCs) derived from human bone marrow (*Lonza, Switzerland*) were cultured as monolayers in Alpha minimum essential medium (α-MEM). This medium was supplemented with 10% FBS and 1% antibiotic-antimycotic mixture, in sterile T175 tissue culture flasks.

Cell seeding was performed as previously described (Canha-Gouveia et al., 2015). Briefly, the P6 hMSCs were trypsinized, centrifuged and resuspended in α-MEM medium. Subsequently, 50 μl of medium containing 1 × 10^5 cells were seeded on top of the scaffold. One hour after cell seeding, culture medium (750 μl) was added to each well and cell-scaffold were incubated 24 h in static conditions. After 24 h, cultures in static conditions were changed to orbital shaking (100 rpm) and kept for 7 days in a humidified atmosphere at 37 °C, containing 5% CO_2, with medium changes every 3 days.

2.3.2.1. Alamar Blue viability assay. Cell viability was determined by Alamar Blue cell viability reagent (*Invitrogen, Massachusetts, USA*). The assay solution was prepared by adding 1/10th of cell viability reagent in α-MEM medium. This solution was added to cell-scaffold for 4 h at 37 °C, containing 5% CO_2, protected from direct light in dynamic conditions. The fluorescence was measured (excitation at $\lambda = 560$ nm; emission at $\lambda = 590$ nm) with a fluorescence spectrophotometer (*Varioskan Flash; Thermo Scientific, Massachusetts, USA*).

2.3.2.2. Cell distribution and morphology. After 7 days of culture, the distribution and morphology of the hMSCs were evaluated using phalloidin/DAPI staining (Silva et al., 2012). Phalloidin labels cytoskeleton (red) whereas the nucleus is stained with DAPI (blue). After cells fixation with 4% paraformaldehyde (PFA; *Sigma, Missouri, USA*) for 30 min at room temperature, the cell-scaffold structure was washed. The scaffold structures were incubated with phalloidin (0.1 μg ml^{-1}; *Sigma, Missouri, USA*) and DAPI (1 μg ml^{-1}; *Sigma, Missouri, USA*) during 30 min. Finally, scaffolds were washed with PBS and observed under a confocal microscope (*Fluoview FV 1000; Olympus, Hamburg, Germany*).

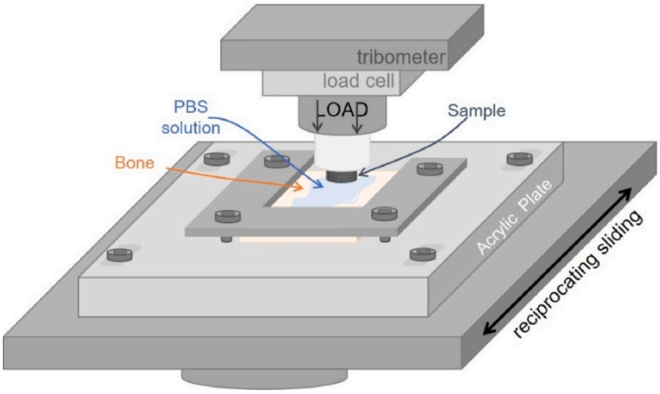

Fig. 2. Schematic illustration of the apparatus for bone-implant interaction experiments.

2.3.3. *Osteogenic differentiation*

Cell differentiation was performed accordingly Westhrin et al. (2015). Briefly, hMSCs were cultured at 37 °C in a humidified atmosphere containing 5% CO_2 in α-MEM, 10% FBS and 1% antibiotic-antimycotic mixture. To induce osteogenic differentiation the media was supplemented with bone morphogenetic protein 2 (BMP-2, 300 mg ml^{-1}, *Millipore, Massachusetts, USA*), ascorbic acid (0.05 mM), dexamethasone (10^{-8} M, *Merck Millipore S.A.S France*) and glycerophosphate (10 mM, *Merck Millipore S.A.S France*). Cells for differentiation purposes were used before passage 8.

2.3.3.1. Alizarin red staining and quantification. Alizarin Red S (AR; *Sigma, Missouri, USA*), an anthraquinone dye, has been widely used to evaluate calcium deposits in cell culture. The AR staining is quite versatile because the dye can be extracted from the stained monolayer of cells and readily assayed. We have applied this quantification assay to the osteogenesis induction of hMSCs.

Cells were cultured in different media, α-MEM and osteogenic differentiation media for 15 days and fixed with PFA 4% and AR staining and quantified for mineral deposit using.

The AR staining was performed after removing the fixative and washing the cell-scaffold 3 times with deionized water (dH_2O). After completely removal of the dH_2O, 40 mM AR was added to each well and incubated at room temperature (RT) for 30 min with gentle orbital shaking. The dye is then removed, and the cell-scaffold were washed 5 times with dH_2O, and photomicrographs were taken in brightfield microscopy (*Leica MZ FLIII; Leica, Germany*).

In order to quantify the calcium mineralization, after photomicrographs acquisition, 10% acetic acid (*Sigma, Missouri, USA*) was added to each well and incubated at RT for 30 min while shaking. Then each cell-scaffold was vortex for 30 s, and heated at exactly 85 °C for 10 min. Samples were then incubated on ice for 5 min, and centrifuged at 20.000 g for 15 min. After centrifugation, supernatant (500 μl) was transfer to a new tube and 10% ammonium hydroxide (200 μl; *Sigma, Missouri, USA*) was added. Aliquots of 150 μl of samples and standards were measured in triplicates in a 96-well plate, and absorbance read at 405 nm with the plate reader (*NanoQuant Infinite M200; Tecan, Switzerland*).

2.4. *Implant-bone interaction tests*

The main purpose of these tests was to mimic, as close to reality as possible, the tribological behavior that occurs during hip implant insertion.

For these experiments, a custom-made apparatus was made,

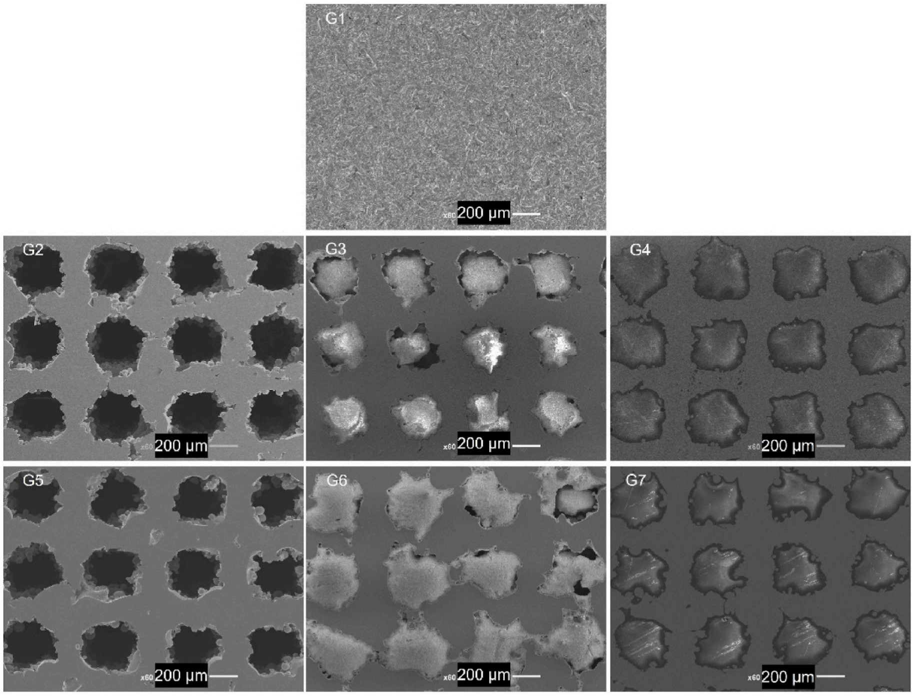

Fig. 3. SEM micrographs of G1-Ti64 SLA, G2-Ti64 SLM, G3-Ti64-βTCP, G4- Ti64-PEEK, G5- NiTi, G6- NiTi- βTCP and G7-NiTi-PEEK specimens. (scale bar: 200 μm).

consisting of a polymeric support for the specimens, rigidly fixed to a load cell, and an acrylic device, fixed to the tribometer, where rectified young bovine femoral bone plates were mounted, as shown schematically in Fig. 2.

The experiments were carried out in a flat-on-flat reciprocating sliding configuration, using a tribometer from *Bruker (UMT-2 model, USA)*.

Three distinct moments were analyzed during these tests, specifically regarding static initial (Si), implantation (I) and final static (Sf) periods.

Briefly, at the moment of implantation, there is a counterforce to the insertion movement, referred as frictional force, being this phenomenon replicated in these bio-tribological tests as static initial.

Then, the moment of implant insertion into the bone cavity happens, where an interaction between the implant and bone occurs (implantation test). This test was performed for a sliding distance of 100 mm in order to mimic the distance commonly used in implant surgeries (Bartolomeu et al., 2019b; Dantas et al., 2017; Wittenberg et al., 2013).

Static final test aims to evaluate the final stability of the implant, i.e., after implant positioning, there is a final frictional force that will dictate the stability of the implant, indicated in literature as primary stability (Costa et al., 2019a; Dantas et al., 2017; Moura et al., 2017).

For all three tests a normal load of 50 N was used, using Phosphate-Buffered Saline (PBS) solution as lubrication fluid, that was kept in a water bath at 37 °C, to mimic the physiological conditions during implantation. After each test, the samples were ultrasonically cleaned in isopropanol for 2 min to remove loose debris resulting from the bio-tribological tests.

2.5. Statistical analysis

Statistical analysis was performed *on GraphPad Prism 8 software (USA)*, by using one way-ANOVA, with differences between groups

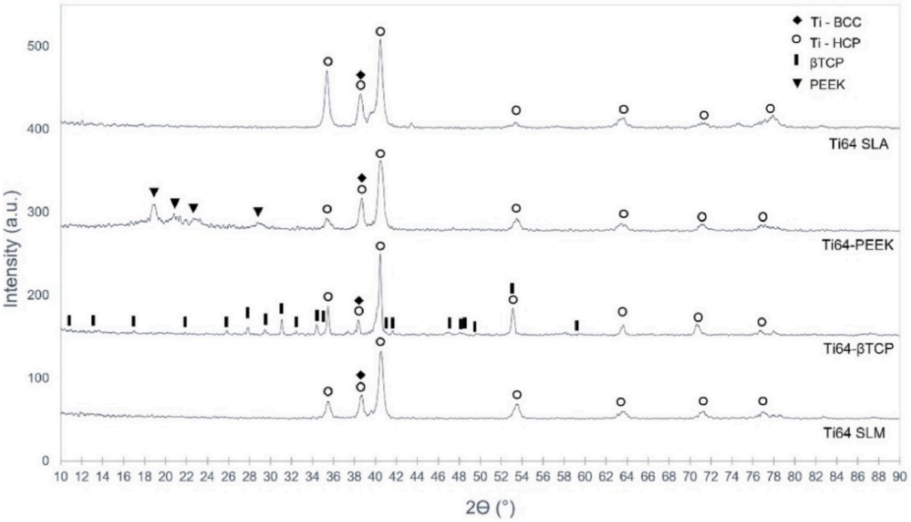

Fig. 4. XRD patterns for Ti64-based specimens.

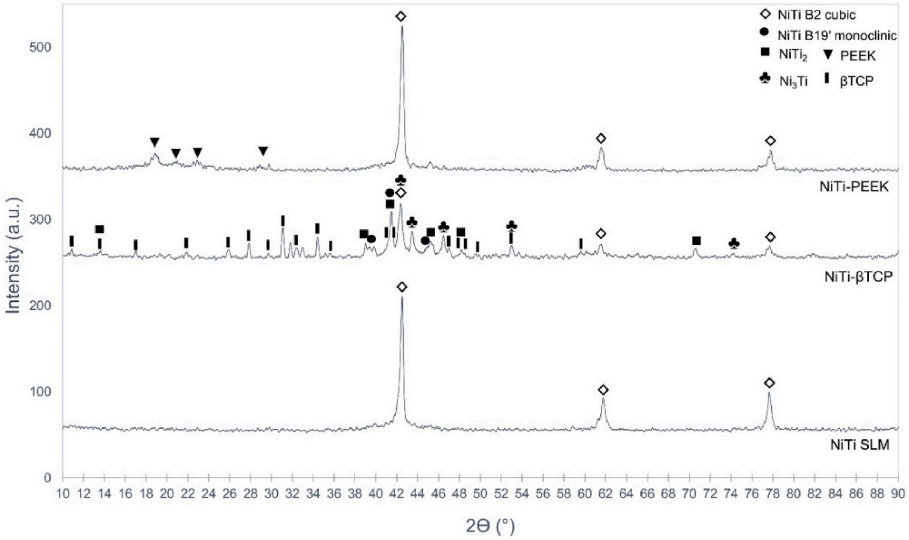

Fig. 5. XRD patterns for NiTi-based specimens.

compared with the post hoc Bonferroni test, to assess the statistically significant differences on bone-implant interactions and *in vitro* results between all the produced groups under study. For each group, an average of 3 repetitions were performed on *in vivo* studies and, for bone-implant interaction tests, experiments ranged between 3 and 4 repetitions. The results were displayed as mean ± standard deviation. Statistical significance was defined for $p < 0.05$ (95% confidence value).

3. Results and discussion

3.1. Morphological and crystallographic characterization

In the present study, NiTi and Ti64 were used as raw materials to manufacture cellular structures by SLM and thus produce mono- and multi-material structures (PEEK or βTCP impregnation as previously described). Fig. 3 shows SEM images of the top surfaces of all the produced mono- and multi-material cellular structured specimens and Ti64 SLA group (G1), representing commercial solution.

When observing Fig. 3 SEM images, some dimensional deviations between the CAD model and the fabricated parts are clearly noticed, namely lower open-cell sizes and larger wall thicknesses on SLM-produced specimens. These cubic-like specimens have open-cell sizes and wall thicknesses, for NiTi structures, of 384.2 ± 21.6 and 187.4 ± 22.9 μm and, for Ti64 structures, of 387.1 ± 33.6 and 178.1 ± 23.8 μm, respectively, similarly to previously reported studies from this group of authors for similar specimens and processing conditions (Bartolomeu et al., 2019c, 2020b, 2019c). In fact, literature extensively reports this phenomenon, inherent to SLM process, related with the partial melting of the powder particles next to the laser melted track. This will consequently lead to thicker walls and consequently smaller open-cells (Bartolomeu et al., 2020b, 2021; Costa et al., 2021; Ran et al., 2018; Taniguchi et al., 2016).

Multi-material groups revealed that the impregnation strategies used for both βTCP or PEEK impregnation were successfully accomplished, as the bioactive/polymeric material is mechanically imprisoned inside the open-cells, making its detachment more difficult to occur, as usually happens when the materials are applied as coatings.

Besides, it is important to highlight that the fabrication of high-quality NiTi specimens is challenging and only a limited group of authors reports its effective fabrication by this technology. In this sense, the NiTi-SLM parts produced in this study, also demonstrate the efficiency of the processing parameters used to produce this material and structures.

Fig. 4 and Fig. 5 show the XRD spectra of Ti64-based and NiTi-based specimens, respectively.

It is known that Ti64 is a β+α alloy, the body-centered cubic (BCC), known as β-phase, and the hexagonal close-packed (HCP) structure, α-phase (Costa et al., 2019b; Melo-Fonseca et al., 2018; Toptan et al., 2019). When observing the Ti64-based specimens XRD spectra (Fig. 4) both phases are detected in all groups. Comparing Ti64 SLA (G1) and Ti64 SLM (G2), despite presenting both phases, the intensities of the peaks slightly differ, which may indicate that the amount of each phase is different. In fact, it is reported in literature that Ti64 microstructure highly depends on the processing cooling rate (Bartolomeu et al., 2016, 2017). While commercial cast Ti64 alloy, G1, is typically characterized by α phase and small amounts of β phase, in SLM, the high temperature gradients and fast cooling rate of the process will lead to the formation of α′ phase (Bartolomeu et al., 2016, 2017, 2019a; Toptan et al., 2019). However, both α or α' phases have a HCP crystalline structure, meaning that they cannot be distinguished in the spectra (Bartolomeu et al., 2020a; Costa et al., 2019b, 2019c; Toptan et al., 2019).

Regarding the NiTi-based specimens (Fig. 5), NiTi group (G5) main peaks corresponds to austenitic phase, cubic – B2 phase (reference pattern no. 03-065-5746). Moreover, martensitic phase is not clearly detected, neither the formation of other intermetallic phases. Conversely, when observing NiTi- βTCP spectra (G6), there are some peaks that can be attributable to martensitic B19' phase, according to pattern no. 00-035-1281. Additionally, $NiTi_2$ and Ni_3Ti peaks can also be detected, considering the XRD reference patterns no. 01-072-0442 and 03-065-2038, respectively. This means that the experimental procedure used for βTCP sintering, where high temperatures are used, may act as a heat treatment step for NiTi. Literature reports that heat treatment between 300 and 500 °C will result in Ni_4Ti_3 phase formation, however, when the temperature increases to higher temperatures, it will lead to Ni_4Ti_3 dissolution into Ni_3Ti (Bhardwaj et al., 2021; Y. Z. Chen et al., 2020; Reddy and Udayashankar, 2016).

Finally, analyzing all the multi-material spectra in both figures (Ti64-βTCP, Ti64-PEEK, NiTi- βTCP and NiTi-PEEK), all the additional peaks detected are attributed to βTCP and PEEK materials, according to βTCP XRD pattern no. 009-0169 and XRD PEEK patterns found in literature (Bartolomeu et al., 2019a; Costa et al., 2019b, 2021).

3.2. In vitro analysis

3.2.1. Cell viability

Right after implantation, a complex cascade of biological events will

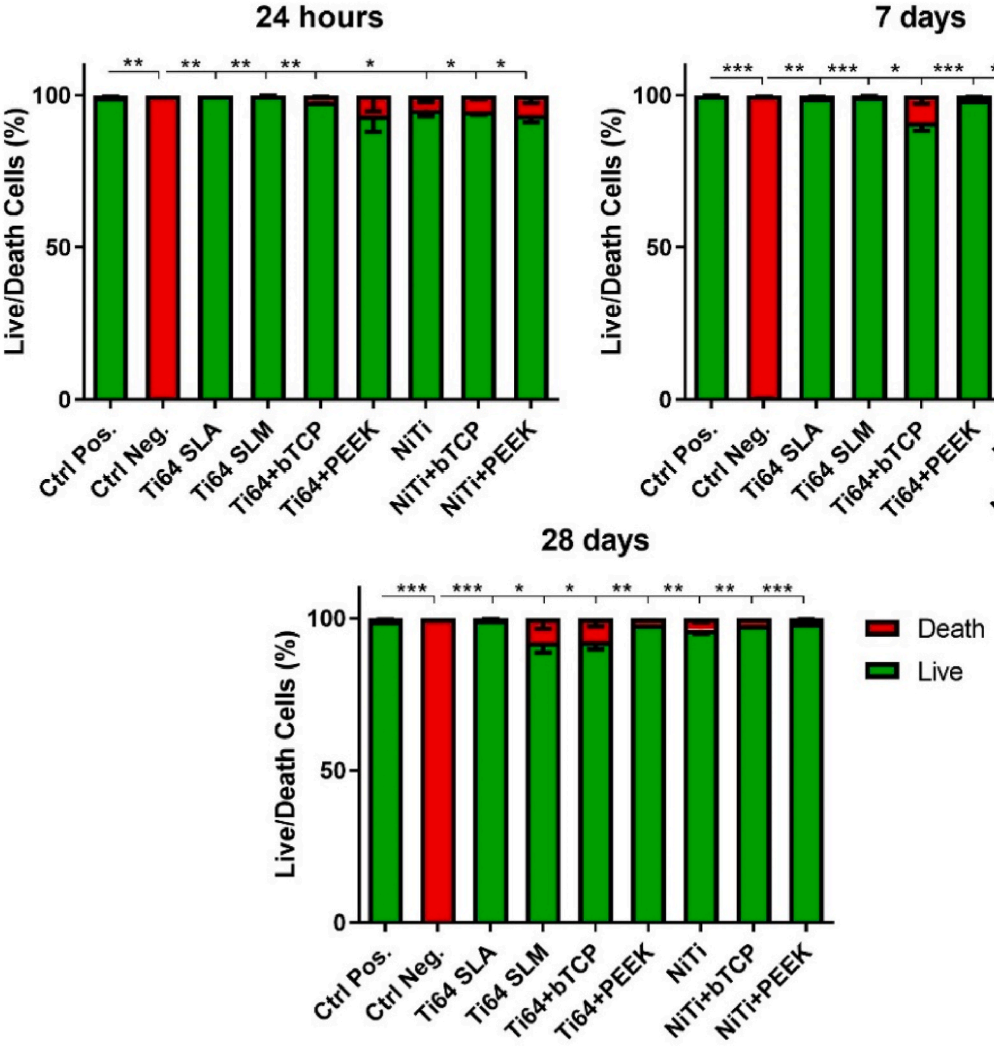

Fig. 6. Cell viability of L929 cells after cultured for 72 h in the specimens' leachables released for the cultured medium during 24 h, 7 and 28 days. Values shown as mean ± SD. * - $p < 0.05$; ** - $p < 0.01$; *** - $p < 0.001$.

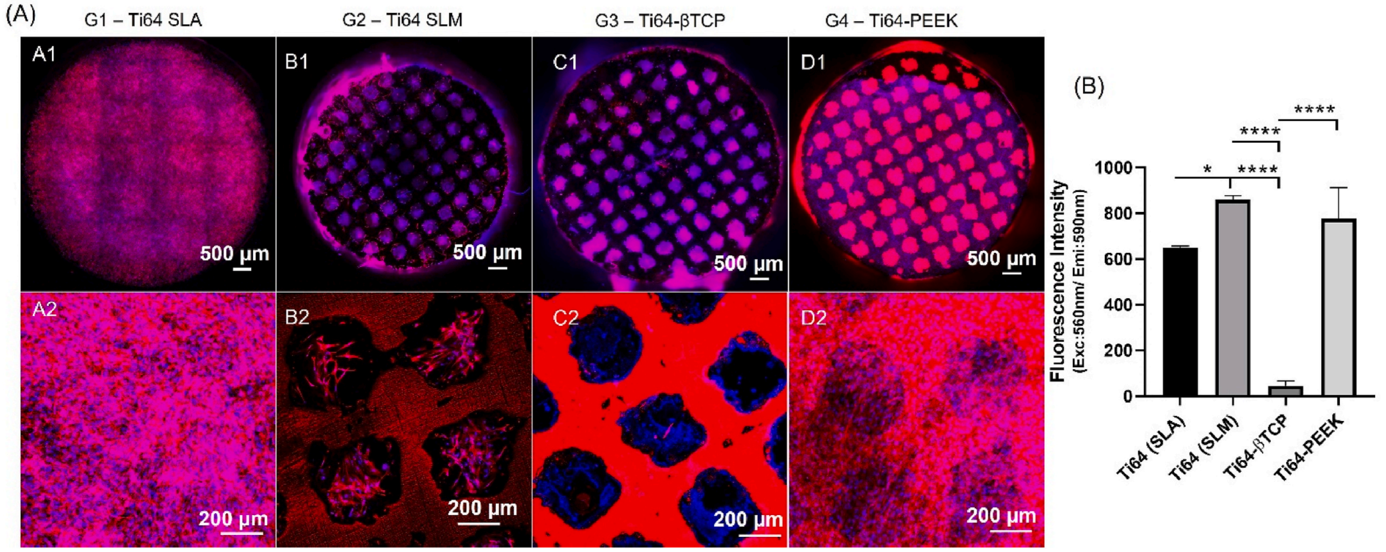

Fig. 7. (A) Fluorescence images of phalloidin/DAPI hMSCs staining after culturing under dynamic conditions for 7 days, at 2 different magnifications. (scale bar: 500 μm); (B) Metabolic activity results for cells cultured in Ti64-based specimens. Values shown as mean ± SD. * - $p < 0.05$; **** - $p < 0.0001$. (scale bar: 200 μm).

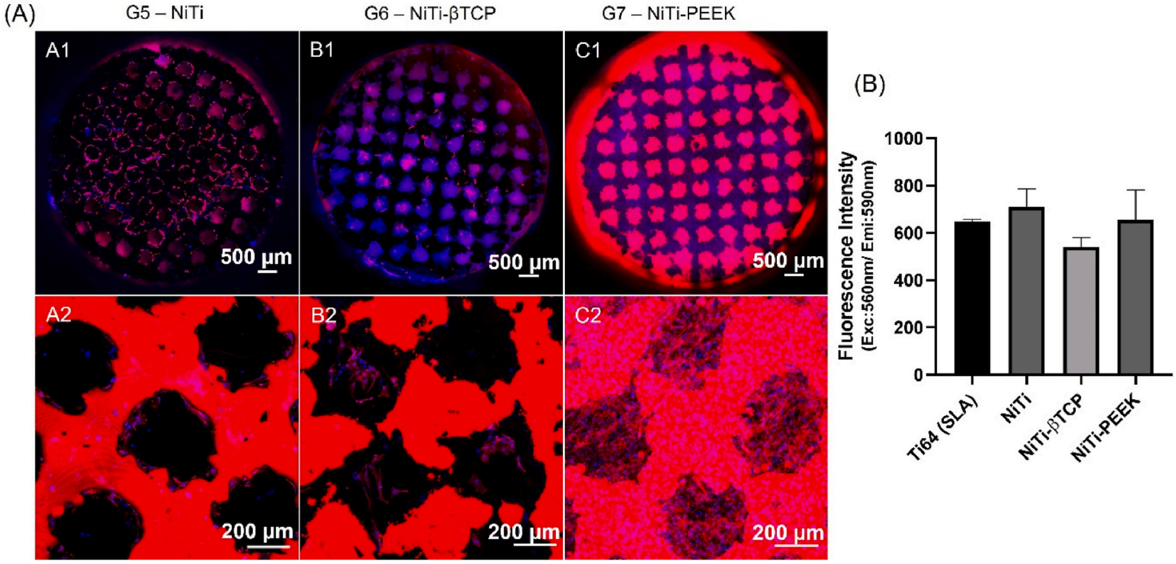

Fig. 8. (A) Fluorescence images of phalloidin/DAPI hMSCs staining after culturing under dynamic conditions for 7 days, at 2 different magnifications. (scale bar: 500 μm); (B) Metabolic activity results for cells cultured in NiTi-based specimens. Values shown as mean ± SD. (scale bar: 200 μm).

occur and, depending on implant's design, material and surface morphology, bone formation on and into its surface will take place. These biological events involve cell attachment, proliferation, differentiation and mineralization (MacBarb et al., 2017; Park et al., 2017). Nevertheless, before all this, it is important to understand if the selected implant material would bring any toxic effect to the host tissue, i.e., if the material can provide a suitable environment for these cellular events to occur.

In this sense, Fig. 6 depicts live/dead results, where the cytotoxic effect of the products released from the specimens during incubation

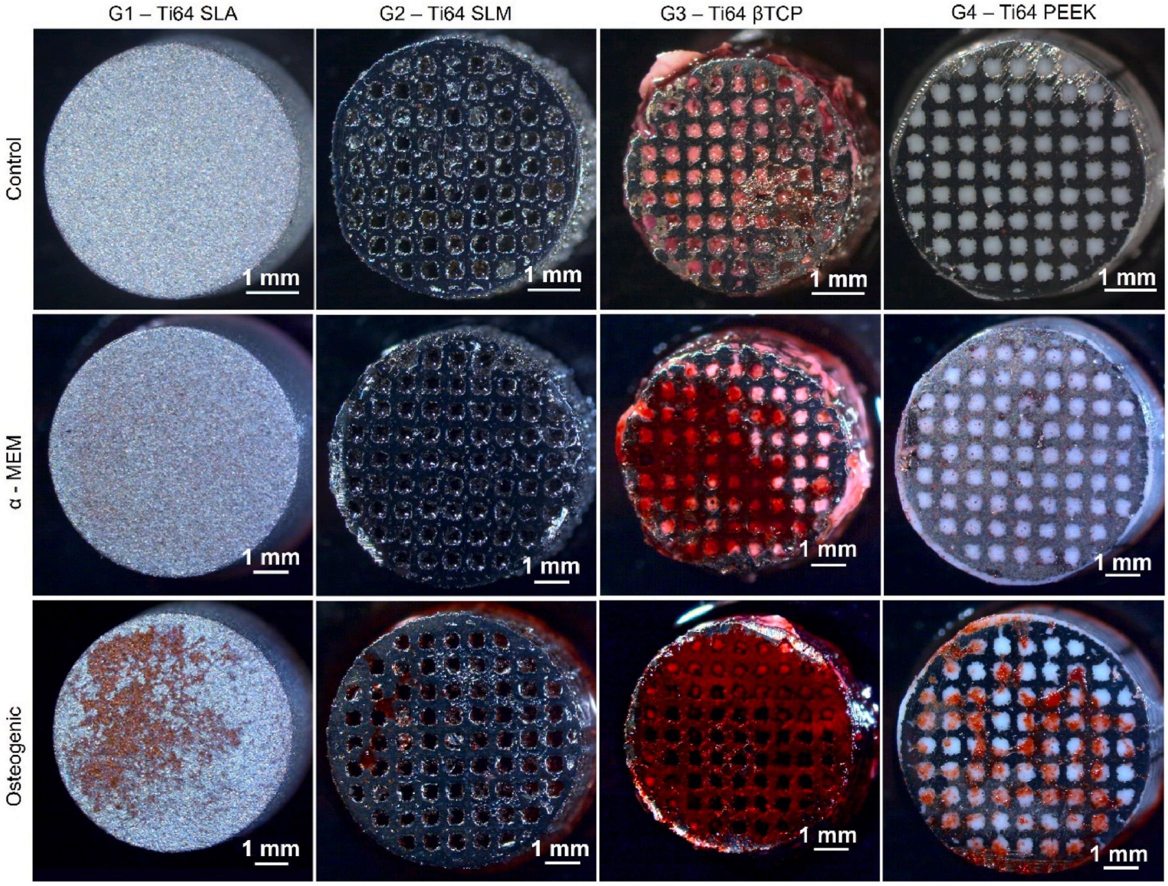

Fig. 9. Alizarin Red staining on Ti64-based specimens on control (no cells), α-MEM and osteogenic media. (scale bar: 1 mm). (For interpretation of the references to color in this figure legend, the reader is referred to the Web version of this article.)

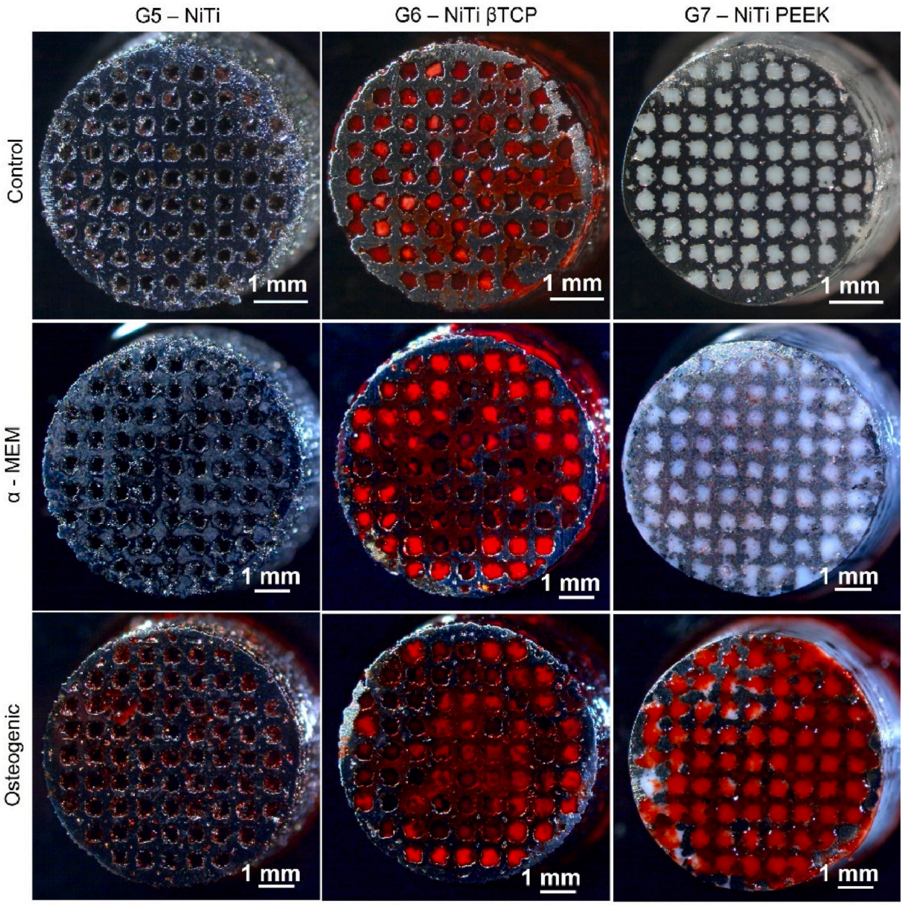

Fig. 10. Alizarin Red staining on NiTi-based specimens on control (no cells), α-MEM and osteogenic media. (scale bar: 1 mm). (For interpretation of the references to color in this figure legend, the reader is referred to the Web version of this article.)

with MEM for the different timepoints were assessed.

As shown in Fig. 6, live/dead results revealed an average percentage of live cells in all groups above 90% even for the higher timepoint (28 days), showing that all the produced specimens did not induced cytotoxicity to cells, with no significant statistical differences found between groups. Nevertheless, at 24 h timepoint, all groups displayed statistically significant differences when compared to the negative control, except Ti64-PEEK group. However, this outcome is not found on the ensuing timepoints.

In this sense, results indicate that the adopted processing strategies (SLM, HP and PS) and the addition of a second material (βTCP or PEEK) had no significant effect on cell cytotoxicity, especially when compared to the available commercial solution (SLA).

3.2.2. *hMSCs adhesion and metabolic activity*

Phalloidin/DAPI and Alamar blue assays were used to assess hMSCs cells morphology and metabolic activity. Fig. 7 and Fig. 8 represent the fluorescence images of the groups (A) and respective metabolic quantification (B) for Ti64-based and NiTi-based groups, respectively. Cell cytoskeleton is represented in red whereas nucleus is stained at blue.

Regarding Ti64-based groups (Fig. 7), results indicate statistically significant differences between Ti64 SLA and SLM groups, with the latter presenting higher cell metabolic activity ($p = 0.0374$), meaning that the cells have a preference over the architecture presented in G2-SLM group.

It is worth mentioning that, despite SLA being widely reported in literature as a surface modification that leads to an improved cellular response, these results revealed a positive effect on the cellular activity on cellular structured group, which has a polished surface condition. Similarly, NiTi-based groups, Fig. 8, indicate higher metabolic activity in NiTi group than Ti64 SLA, although statistical analysis revealed no differences. This outcome can be related with higher exposed surface area found in SLM groups, when compared to SLA (G1). This open interconnected architecture provides a suitable environment for a free-flow of the culture media and for the delivery to cells of the necessary nutrients and oxygen for them to proliferate.

The fluorescence images of cell morphology indicate the actin cytoskeleton (red color) stained by Phalloidin, while cell nuclei are visible in blue (stained by DAPI). In both figures (Figs. 7 and 8) it is visible, especially at higher magnification, that cells migrate and proliferate inside the open-cells, corroborating the metric results. Despite cell density on G1-Ti64 SLA is higher, this is observed in a single plane, conversely to the mono-material cellular groups (G2 and G5) where cells can be found inside the open-cells, a great indicator for further bone ingrowth. These findings are in accordance with studies found in literature, that indicate that a porous, interconnected network enhance cell migration, proliferation and differentiation (Park et al., 2017; Ran et al., 2018; Yang et al., 2017). Ran et al. (2018) stated that these porous structures facilitate nutrients and oxygen transport, crucial aspects for vascularization and osteogenesis for further bone ingrowth that, subsequently, will increase implant-bone fixation.

When observing multi-material Ti64-based groups, no significant differences were found between mono-material (G1 and G2) and Ti64-PEEK group (G4), however a pronounced metabolic activity decrease was observed in Ti64-βTCP (G3), that were statistically different from the remaining groups ($p < 0.0001$). A similar trend was observed on NiTi-based specimens, however no significant differences were found among groups. Fluorescence images may help clarify such results, since in G3-Ti64 βTCP group, lower cell density was found adhered to the

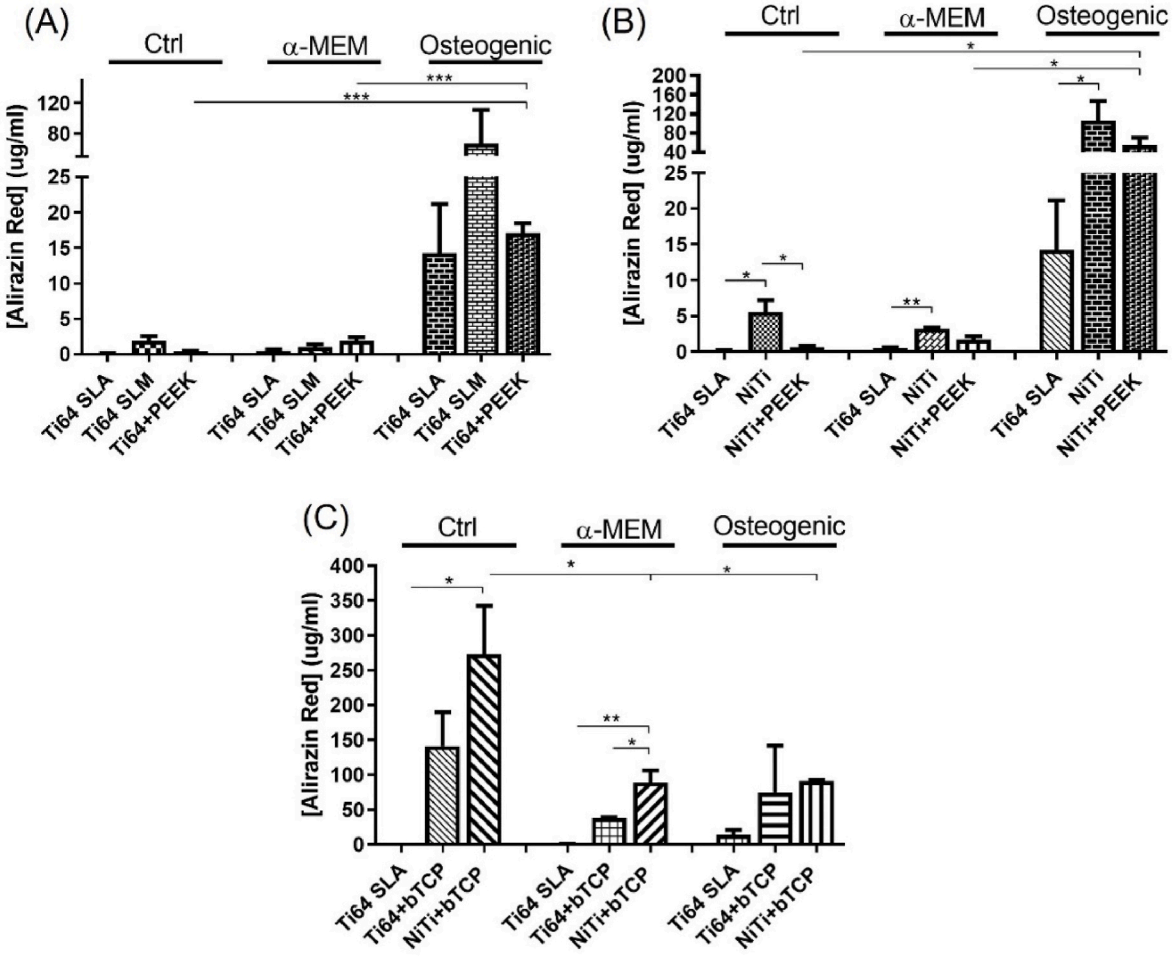

Fig. 11. Alizarin Red quantification for (A) Ti64-based, (B) NiTi-based groups and (C) Groups with βTCP for the different media after 15 days cell culture. Values shown as mean ± SD. * - $p < 0.05$; ** - $p < 0.01$; *** - $p < 0.001$.

specimen, when compared to other groups, while in G6-NiTi βTCP this observation was not as pronounced.

Regarding PEEK-impregnated specimens (G4 and G7), despite the open cells were fully impregnated with the polymeric material, higher density of cells was found, which may be an indicator that PEEK has a positive effect on cell adhesion.

3.2.3. *hMSCs differentiation and mineralization*

After cell viability and hMSCs adhesion and metabolic activity, cell differentiation and mineralization were evaluated by Alizarin Red assay tests.

Alizarin red (AR), as described, was used to detect calcium deposits on the specimens and detect extracellular matrix mineralization by mature osteoblasts (Backes et al., 2021; Lei et al., 2022). Fig. 9 and Fig. 10 show images of alizarin red staining after cell culture for 15 days in Ti64-based and NiTi-based groups, respectively. For comparison purposes, the assay was performed in three different conditions with cells being cultured using an α-MEM or an osteogenic media, and a control condition where no cells were used, aiming to evaluate the reliability of the test. Results regarding quantitative AR analysis are shown in Fig. 11.

When observing Alizarin Red staining it is possible to conclude that, in the osteogenic medium, all the produced specimens, after 15 days, presented some degree of mineralization. AR quantifications corroborate this outcome since both Ti64- and NiTi-based groups (Fig. 11 (A) and (B), respectively), presented higher mineralization in the osteogenic medium when compared to α-MEM medium, as expected. This trend is visible in all groups, although significant differences were only found on Ti64-PEEK ($p = 0.0002$) and NiTi-PEEK ($p = 0.0158$) groups.

Similarly, it is also visible that, when comparing the control medium, higher values of mineralization were detected on osteogenic medium, although no significant differences were found, except for Ti64-PEEK ($p = 0.0002$) and NiTi-PEEK ($p = 0.0147$). It is expected that, in control assays, no mineralization occurs once, in these samples, no cells were included. However, an increased AR was found on Ti64 SLM and NiTi groups, being statistically different, in the NiTi-based specimens, when compared to Ti64 SLA ($p = 0.0327$) and NiTi-PEEK ($p = 0.0436$) groups. This outcome should be related with these groups' architecture, since the interconnected porous structure will make the cleaning step of the protocol difficult.

By observing AR results for α-MEM medium, an increased AR for Ti64- and NiTi-SLM groups (G2 and G5) was observed, when compared to SLA, with statistical differences found for the later ($p = 0.0097$). Additionally, an increased AR for PEEK-impregnated specimens was found, although not having significant differences, in comparison to SLA.

When regarding the osteogenic media, no statistical differences were found among groups, except NiTi that displays higher AR when compared to Ti64 SLA ($p = 0.0143$). However, a similar trend can be detected, with higher AR found for mono-material SLM groups and multi-material PEEK-impregnated ones, when compared to SLA. These results are in agreement with AR staining, where higher mineralization can be detected in PEEK-impregnated groups, in both osteogenic media and α-MEM, than in SLA. In SLM groups, these findings are not so visible

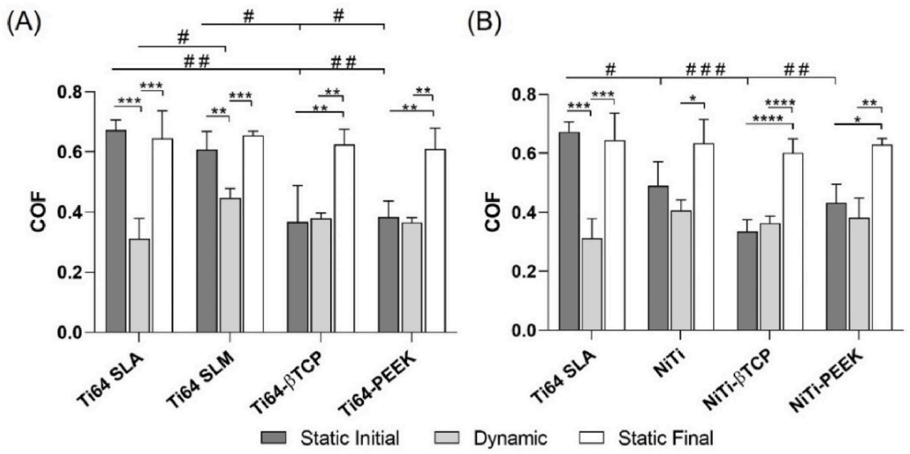

Fig. 12. Coefficient of friction (COF) values for static initial, dynamic and static final tests, for (A) Ti64-based specimens and (B) NiTi-based specimens, worn against bone plate. Values shown as mean ± SD. * or # - $p < 0.05$; ** or ## - $p < 0.01$; *** or ### - $p < 0.001$.

to detect on the specimen's surface, indicating that mineralization may be occurring inside the structures.

It is important to highlight that, in α-MEM, PEEK-impregnated groups already present some degree of mineralization, compared to the remaining groups, suggesting its enhanced ability to induce mineralization, without the addition of the osteogenic elements.

In fact, by observing Figs. 9 and 10, apparently, the groups with high degree of mineralization were the ones having βTCP, as the surface is homogeneously distributed with deposits of calcium. As seen in Fig. 11 (C), higher average values of mineralization with and without osteogenic factors were found, when compared to the remaining groups, in exception to NiTi-based groups in the osteogenic media, still being the second highest group.

Compared to Ti64 SLA group, statistical analysis only revealed significant differences for NiTi-βTCP group, with higher AR values found for the later ($p = 0.0085$), although the tendency for higher values on βTCP groups is perceivable.

However, it is important to highlight that βTCP already has calcium in its composition, and since AR detects calcium deposits, this could lead to a spontaneous dyeing. In this sense, the control medium results (where no cells were added) help on understanding the effect of this spontaneous dyeing in mineralization.

Results, both from AR staining and quantification, indicate that this test is not suitable for quantifying mineralization on calcium-based specimens once it is possible to identify "mineralization" even in the groups that were not in contact with cells, although significance was only detected on NiTi-βTCP group. In this sense, these results demonstrated that AR staining should not be used to quantify mineralization in the scaffolds having βTCP. However, when used, the control assay, without cells, must be carried out with the same culture times as the remaining culture media, and the results must be presented considering the results obtained from the control.

Overall, results revealed that the scaffolds herein tested did not presented cytotoxic effects and the proposed design for introducing a porous interconnected structure enhances the overall cellular response in terms of metabolic activity, differentiation, and mineralization, when compared to Ti64 SLA. As mentioned, this is related with the ability of such structures to significantly enhance exposed surface area while providing space for a free-flow of oxygen and nutrients for cellular events to occur allowing further bone formation and ingrowth.

Moreover, as for multi-material specimens, the addition of PEEK has shown an overall positive cellular response, in comparison to Ti64 SLA, presenting an equal or better behavior than SLM groups.

Finally, the addition of βTCP did not bring any advantage in terms of improving cellular behavior. Conversely, several studies in literature report the beneficial effects of adding calcium phosphates for better adhesion and enhanced differentiation and mineralization, when compared to specimens without these materials (Backes et al., 2021; Harb et al., 2020; Park et al., 2017; Peñarrieta-juanito et al., 2018; Zheng et al., 2021). In the present study, almost all metrics displayed non-significant differences or lower values when adding this material.

MarcBarb et al. (MacBarb et al., 2017) reported similar results when comparing the response of human osteoblasts in additive manufactured implants with traditional machined ones, with and without hydroxyapatite coating. In their study, results revealed that almost all metrics were decreased with the addition of hydroxyapatite and this outcome could be related with the bioactive crystallinity, since, highly crystalline hydroxyapatite is usually associated with lower dissolution that in turn negatively affect cellular adhesion (MacBarb et al., 2017; Müller et al., 2021).

Backes et al. (2021) also reported that using higher concentrations of βTCP would inhibit cell proliferation, based on previous reported studies (Liu et al., 2009; Nakagawa et al., 2013). It is discussed that higher amount of this bioactive material will decrease calcium and phosphate concentrations in the medium and, in turn, ions will be absorbed on the bioactive surface during crystalline growth and mineralization process. On the other hand, if used in lower concentrations, this material will promote cell growth as proteins are being absorbed and cells bonded to the surface. Nakagawa et al. (2013) reported that high concentration of βTCP inhibited proliferation and increased dead cells of MSCs, pointing out some possible reasons, namely: proliferation and viability of MSCs could be affected by low calcium and phosphorus concentration in the medium; βTCP excessively absorbed by the MSCs can be toxic; and the MSC transition from the proliferative to the differential phase may have resulted in inhibition of proliferation (in a calcification medium, only osteogenic lineage MSCs live).

This group of authors, on a previously published paper (Costa et al., 2019c) also revealed that the addition of bioactive βTCP will lead to an alkalinization of the medium, that is detrimental for hMSCs proliferation and osteogenic differentiation. It was reported that the impregnation of the open-cells will hamper fluid flow, and the culture medium will be stagnated inside the structures and saturated with the dissolution products, increasing the pH and, consequently, enhancing the toxicity of the medium.

In this sense, literature is controversial when discussing *in vitro* response of bioactive materials, and this same response could vary depending on several aspects: type of cells used and corresponding culturing needs, specimens production methods, surface conditions, etc (MacBarb et al., 2017). In this regard, as a suggestion for future studies, it would be interesting to assess *in vitro* performance of multi-material

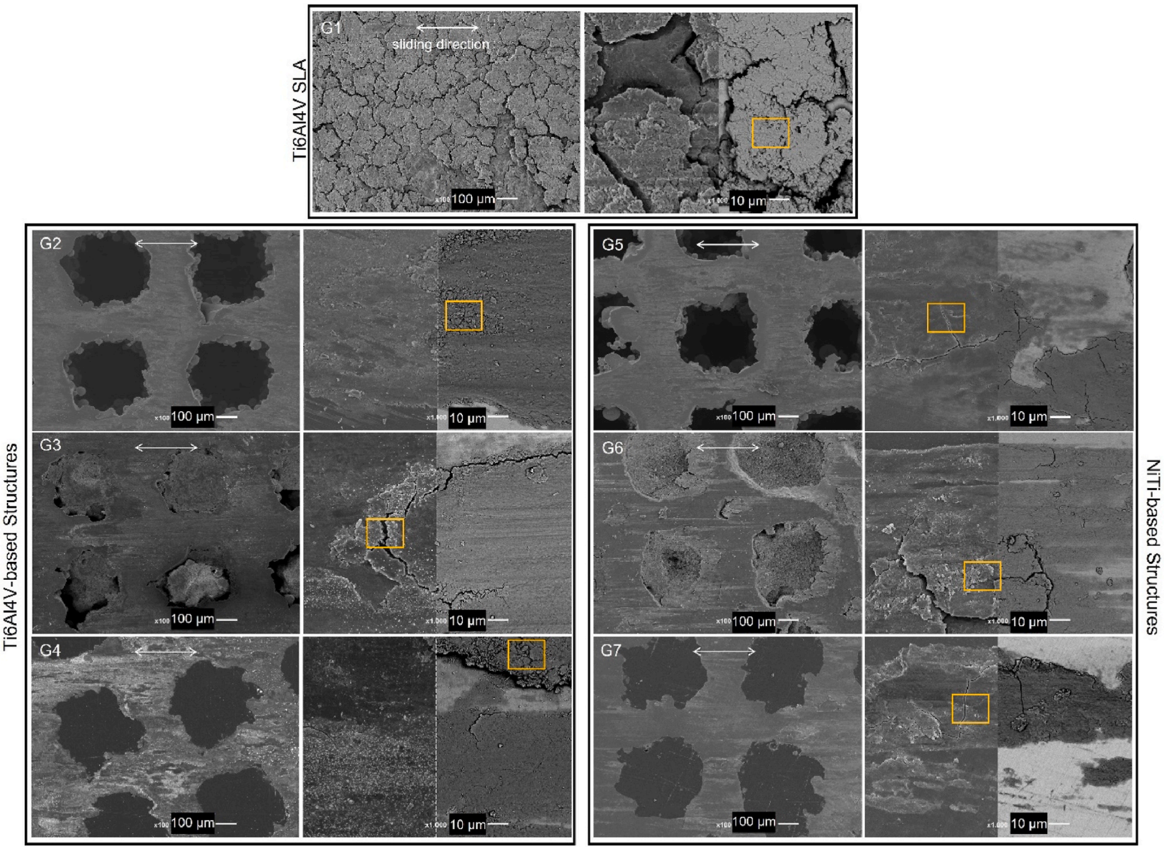

Fig. 13. SEM images of worn surfaces for G1-Ti64 SLA, G2-Ti64 SLM, G3-Ti64-βTCP, G4- Ti64-PEEK, G5- NiTi, G6- NiTi- βTCP and G7-NiTi-PEEK groups. Marked yellow squares represent EDS region (see Table 2). (scale bar left: 100 μm and right: 10 μm). (For interpretation of the references to color in this figure legend, the reader is referred to the Web version of this article.)

structures in which the bioactive is used as a thin-coating on the outer and inner surfaces of the metallic structures to provide both the adequate media inside the open-cells and bioactivity for an enhanced osteoinduction while offering available space for cells to proliferate and bone to grow inside these structures. Furthermore, it is also important to perform *in vivo* experiments in further studies, to understand the behavior of such materials in a closer-to-reality conditions.

3.3. Implant-bone interaction tests

When regarding implants implantation process, it is important to guarantee a good fixation to the surrounding bone for the osseointegration process to occur. For that purpose, the stability of an implant is assured if primary and consequently secondary stability are guaranteed.

During implantation, the press-fit process is responsible for assuring implant anchorage to the bone being, therefore, mechanically fixed and achieving primary stability (Bartolomeu et al., 2019b; Dantas et al., 2017; Moura et al., 2017; Tiainen et al., 2019). Afterwards, a cascade of biological events will occur and allow bone to grow at the implant-bone interface, guaranteeing long-term stability of the implant (secondary stability) (Bartolomeu et al., 2019b; Dantas et al., 2017; Moura et al., 2017).

In this sense, studying the implant-bone interaction during implantation is extremely important to assess implant adhesion and stability after the procedure (primary stability). Fig. 12 shows the average static initial, implantation and static final coefficient of friction values, obtained during implant-bone interaction tests against bone plates.

When analyzing static initial COF for Ti64-based groups (Fig. 12 (A)) it is possible to observe that, from all groups, Ti64 SLA was the one with highest value, being the difference statistically significant from Ti64-βTCP ($p = 0.0035$) and Ti64-PEEK ($p = 0.0033$) groups. Similarly, higher static initial COF was found for G1 (Ti64 SLA), when compared to the remaining NiTi-based groups, Fig. 12 (B), with p values for NiTi, NiTi-βTCP and NiTi-PEEK being 0.0273, 0.0006 and 0.0055, respectively.

It has been proved that the tribological behavior is highly influenced by the surface properties of the materials (surface design, roughness) and by the testing conditions namely, applied load, lubrication conditions, etc (Bartolomeu et al., 2019b; Faria et al., 2020; Madeira et al., 2020; Moura et al., 2017).

When regarding the static coefficient of friction, surface chemical composition and morphology are crucial factors to consider. In this particular case, as mentioned, Ti64 SLA group (G1) exhibits a moderate surface roughness, contrary to the other groups where the walls of the structures have a polished surface finishing. This means that, before sliding, the contact between G1 specimens and the bone was through the peaks of the surface, meaning that higher forces were required to initiate the movement.

When comparing the mono-material SLM group with multi-material ones, it is found that the former displayed higher static initial COF, being statistically different for Ti64-based groups. Despite NiTi group was not found to be statistically different than multi-material NiTi-based groups, this tendency of higher static COF for mono-material group can also be observed. Despite all these structures have polished surface finishing, mono-material structures, having open-cells, have lower contact area than multi-material ones, where the cells are filled with bioactive or polymeric material. This can explain the higher static initial COF, once the lower contact area leads to higher contact pressure and higher forces to start motion.

When regarding dynamic tests COF, no significant differences were

Table 2
Chemical composition (in wt. %) of the material transfer zones in all specimens.

Sample Group	Ca	P	Ti	Al	O	C	Others
G1: Ti64 SLA	27.2	14.5	1.5	–	38.3	16.6	1.9
G2: Ti64 SLM	21.4	11.4	10.6	0.7	39.8	13.4	2.7
G3: Ti64-βTCP	21.6	11.4	8.9	0.7	35.9	16.9	4.5
G4: Ti64-PEEK	23.6	13.3	1.2	–	37.9	17.2	6.8
G5: NiTi	27.2	15.1	2.2	–	39.9	12.4	3.3
G6: NiTi-βTCP	25.9	13.1	6.2	–	33.7	15.1	6
G7: NiTi-PEEK	25.5	15.6	1.5	–	37.5	16	3.9

found between groups, except for Ti64 SLM (G2) and Ti64 SLA (G1) with higher dynamic COF for the former ($p = 0.015$). Nevertheless, average values indicate an overall trend, with the lowest COF displayed by G1. When sliding starts, after few cycles, surface peaks are polished and the valleys filled with detached bone now adhered to the surface, which will minimize the topography effect and reduce the coefficient of friction.

Theoretically, it is usual that the dynamic COF is lower than the static, however, statistical differences were only found in static initial COF for G1 and G2 group, despite average values show this trend. However, this is not observed for multi-material structures impregnated with βTCP, possibly due to bioactive detachment from the open cells, during sliding, releasing harder particles that will interact with the mating surfaces.

When observing final static COF values, it can be concluded that, for all groups, higher values were obtained when compared to dynamic COF, being statistically different. This indicates that a good adhesion to bone has occurred, for all groups, with no significant differences between them.

Fig. 13 show SEM micrographs of the worn surfaces, using two different magnifications, for all groups specimens. Chemical analysis was also performed to assess bone transfer to the specimens and results from the marked yellow zones in Fig. 13 can be observed in Table 2. In this figure, the sliding direction is indicated by the white arrow.

By observing the higher magnification images of the specimens in Fig. 13, it is possible to distinguish, by atomic contrast, two zones in dark and light gray, corresponding to the bone adhered to the surface and to the metal surface, respectively. In this sense, it can be concluded that adhesion occurred in all the tested groups, due to bone adherence to the surface, but also abrasion since grooves aligned with the sliding direction are visible in all micrographs. Adhesion is also proven by EDS analysis since, in all groups, Ca and P (corresponding to bone) are clearly detected.

During sliding, the released bone debris will adhere to the specimens' surface and form a new compact tribolayer that will have a major contribution to the tribological behavior. In fact, this newly formed bone layer will smooth the specimens' surface and lower the coefficient of friction. In this study, it is visible that the adhered bone in G1 covers almost the entire surface whilst in the remaining groups this new bone layer extension is lower. As mentioned, this behavior can be explained by G1 specimens surface roughness, higher than that of polished groups, but also the presence of open cells that, during sliding, may act as containers for bone wear debris to be collected.

These results indicate that, regarding primary stability, despite not displaying significant differences when compared to the commercially available solution (G1), the benefits arising from the proposed solutions,

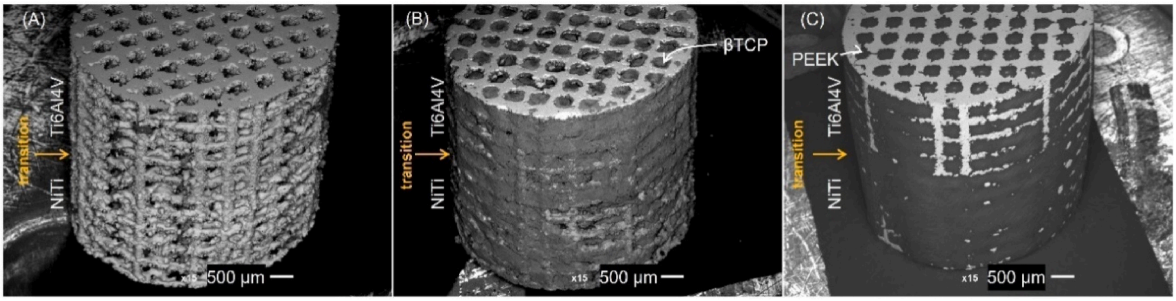

Fig. 14. SEM micrographs of bimetallic specimens isometric perspective (A) NiTi–Ti64, (B) NiTi–Ti64-βTCP and (C) NiTi–Ti64-PEEK. (scale bar: 500 µm).

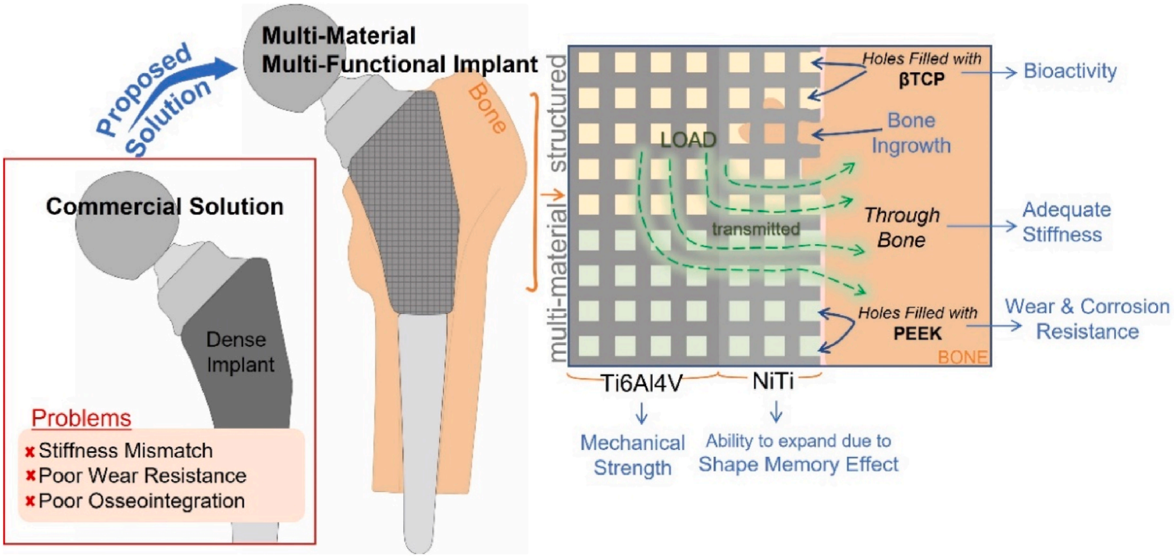

Fig. 15. Design concept of multi-material multi-functional hip implant solution.

in terms of allowing bone ingrowth and elastic modulus tailoring make them extremely suitable and attractive for orthopedic applications.

Finally, bimetallic specimens were also produced and are shown in Fig. 14. From these images, it is possible to perceive, especially in the bimetallic group (NiTi–Ti64), the transition between NiTi and Ti64 cellular structure. This was successfully achieved, with a good bond between the two different materials, which, once again, validates the strategy and the processing parameters used. Similarly, the impregnation process was also validated, once the bioactive and polymeric materials were successfully impregnated into the open-cells.

These solutions were fabricated as a proof-of-concept for new approaches to bring multi-functionality to the final component, as schematically represented in Fig. 15. In detail, by introducing porosity it is expected to enhance the bone-implant mechanical anchoring by promoting bone ingrowth and also tailor the elastic properties of the material. Bartolomeu et al. (Bartolomeu et al., 2019c, 2020b, 2019c) reported an elastic modulus for Ti64 and NiTi structures of ≈ 16 GPa and ≈ 4 GPa, respectively. Despite NiTi cellular structure has lower elastic modulus, when compared to that of cortical bone (ranges between 10 and 30 GPa) (Bartolomeu et al., 2019c, 2020a, 2020b; Costa et al., 2021), it is intended to use this material as an outer layer of the implant, being the inner part composed of structured Ti64, that displays an elastic modulus within the referred cortical bone range.

Moreover, the bioactive and polymeric materials can be added to a final multi-material solution allocated in different regions of the implant, where different requirements exist.

Overall, these solutions are developed thinking of a broader goal, that is the fabrication of patient-specific implants that can fulfill local requirements by using different architectures and materials combinations.

4. Conclusions

- Ti64 and NiTi cellular structures were successfully produced by Selective Laser Melting.
- βTCP and PEEK impregnation inside these structures was effectively performed by Press and Sintering for the previous and Hot Pressing for the latter, with the bioactive/polymeric material being mechanically imprisoned inside the open-cells.
- *In vitro* results showed that no significant cell cytotoxicity was elicited by any of the groups. SLM mono-material structures displayed an enhanced overall cellular response (higher metabolic activity and mineralization) when compared to bulk SLA.
- Compared to Ti64 SLA, PEEK addition provided an improved cell adhesion, metabolic activity and, subsequently, cellular differentiation and mineralization whilst βTCP seems to bring no advantage regarding cell behavior (lower metabolic activity).
- Bone-implant interaction tests revealed that Ti64 SLA was the group with higher initial static coefficient of friction, nevertheless, no significant differences were found regarding final static coefficient of friction, indicating similar primary stability among groups.
- Overall, the solutions here proposed can be used to provide adequate elastic properties that match with cortical bone (cellular structures), while assuring adequate cellular response without compromising the overall primary stability of the implant.

CRediT authorship contribution statement

M.M. Costa: Writing – original draft, Visualization, Methodology, Investigation, Formal analysis. **R. Lima:** Methodology, Investigation, Formal analysis. **N. Alves:** Resources. **N.A. Silva:** Writing – review & editing, Resources. **M. Gasik:** Writing – review & editing. **F.S. Silva:** Writing – review & editing, Supervision, Conceptualization. **F. Bartolomeu:** Writing – review & editing, Supervision, Methodology, Conceptualization. **G. Miranda:** Writing – review & editing, Supervision, Funding acquisition, Conceptualization.

Declaration of competing interest

The authors declare that they have no known competing financial interests or personal relationships that could have appeared to influence the work reported in this paper.

Acknowledgments

This work was supported by FCT (Fundação para a Ciência e a Tecnologia) through the grant SFRH/BD/140191/2018, the work contract CEECIND/04794/2007, the project PTDC/EME-EME/1442/2020 (Add2MechBio) and the project NORTE-01-0145-FEDER-029968. This work has been also funded by ICVS Scientific Microscopy Platform, member of the national infrastructure PPBI - Portuguese Platform of Bioimaging (PPBI–POCI-01-0145-FEDER-022122). Additionally, it was developed within the scope of the project CICECO-Aveiro Institute of Materials, UIDB/50011/2020, UIDP/50011/2020 & LA/P/0006/2020, financed by national funds through the FCT/MEC (PIDDAC). Finally, this work was supported by FCT national funds, under the national support to R&D units grant, through the reference projects UIDB/04436/2020, UIDP/04436/2020, UIDB/50026/2020 and UIDP/50026/2020.

References

Alabort, E., Barba, D., Reed, R.C., 2019. Design of metallic bone by additive manufacturing. Scripta Mater. 164, 110–114. https://doi.org/10.1016/j.scriptamat.2019.01.022.

Backes, E.H., Fernandes, E.M., Diogo, G.S., Marques, C.F., Silva, T.H., Costa, L.C., Passador, F.R., Reis, R.L., Pessan, L.A., 2021. Engineering 3D printed bioactive composite scaffolds based on the combination of aliphatic polyester and calcium phosphates for bone tissue regeneration. Mater. Sci. Eng. C 122, 111928. https://doi.org/10.1016/j.msec.2021.111928.

Bartolomeu, F., Buciumeanu, M., Costa, M.M., Alves, N., Gasik, M., Silva, F.S., Miranda, G., 2019a. Multi-material Ti6Al4V & PEEK cellular structures produced by Selective Laser Melting and Hot Pressing: a tribocorrosion study targeting orthopedic applications. J. Mech. Behav. Biomed. Mater. 89, 54–64. https://doi.org/10.1016/j.jmbbm.2018.09.009.

Bartolomeu, F., Buciumeanu, M., Pinto, E., Alves, N., Silva, F.S., Carvalho, O., Miranda, G., 2017. Wear behavior of Ti6Al4V biomedical alloys processed by selective laser melting, hot pressing and conventional casting. Trans. Nonferrous Metals Soc. China 27, 829–838. https://doi.org/10.1016/S1003-6326(17)60060-8.

Bartolomeu, F., Costa, M.M., Alves, N., Miranda, G., Silva, F.S., 2021. Selective Laser Melting of Ti6Al4V sub-millimetric cellular structures: prediction of dimensional deviations and mechanical performance. J. Mech. Behav. Biomed. Mater. 113, 104123 https://doi.org/10.1016/j.jmbbm.2020.104123.

Bartolomeu, F., Costa, M.M., Alves, N., Miranda, G., Silva, F.S., 2020a. Additive manufacturing of NiTi-Ti6Al4V multi-material cellular structures targeting orthopedic implants. Opt Laser. Eng. 134, 106208 https://doi.org/10.1016/j.optlaseng.2020.106208.

Bartolomeu, F., Costa, M.M., Alves, N., Miranda, G., Silva, F.S., 2020b. Engineering the elastic modulus of NiTi cellular structures fabricated by selective laser melting. J. Mech. Behav. Biomed. Mater. 110, 103891 https://doi.org/10.1016/j.jmbbm.2020.103891.

Bartolomeu, F., Costa, M.M., Gomes, J.R., Alves, N., Abreu, C.S., Silva, F.S., Miranda, G., 2019b. Implant surface design for improved implant stability – a study on Ti6Al4V dense and cellular structures produced by Selective Laser Melting. Tribol. Int. 129, 272–282. https://doi.org/10.1016/j.triboint.2018.08.012.

Bartolomeu, F., Faria, S., Carvalho, O., Pinto, E., Alves, N., Silva, F.S., Miranda, G., 2016. Predictive models for physical and mechanical properties of Ti6Al4V produced by Selective Laser Melting. Mater. Sci. Eng. 663, 181–192. https://doi.org/10.1016/j.msea.2016.03.113.

Bartolomeu, F., Fonseca, J., Peixinho, N., Alves, N., Gasik, M., Silva, F.S., Miranda, G., 2019c. Predicting the output dimensions, porosity and elastic modulus of additive manufactured biomaterial structures targeting orthopedic implants. J. Mech. Behav. Biomed. Mater. 99, 104–117. https://doi.org/10.1016/j.jmbbm.2019.07.023.

Bhardwaj, A., Ojha, M., Garudapalli, A., Gupta, A.K., 2021. Microstructural, mechanical and strain hardening behaviour of NiTi alloy subjected to constrained groove pressing and ageing treatment. J. Mater. Process. Technol. 294, 117132 https://doi.org/10.1016/j.jmatprotec.2021.117132.

Canha-Gouveia, A., Costa-Pinto, A.R., Martins, A.M., Silva, N.A., Faria, S., Sousa, R.A., Salgado, A.J., Sousa, N., Reis, R.L., Neves, N.M., 2015. Hierarchical scaffolds enhance osteogenic differentiation of human Wharton's jelly derived stem cells. Biofabrication 7, 35009. https://doi.org/10.1088/1758-5090/7/3/035009.

Chen, S.Y., Huang, J.C., Pan, C.T., Lin, C.H., Yang, T.L., Huang, Y.S., Ou, C.H., Chen, L.Y., Lin, D.Y., Lin, H.K., Li, T.H., Jang, J.S.C., Yang, C.C., 2017. Microstructure and mechanical properties of open-cell porous Ti-6Al-4V fabricated by selective laser melting. J. Alloys Compd. 713, 248–254. https://doi.org/10.1016/j.jallcom.2017.04.190.

Chen, Y., Sun, S., Zhang, T., Zhou, X., Li, S., 2020. Effects of post-weld heat treatment on the microstructure and mechanical properties of laser-welded NiTi/304SS joint with Ni filler. Mater. Sci. Eng. 771, 138545 https://doi.org/10.1016/j.msea.2019.138545.

Chen, Z., Yan, X., Yin, S., Liu, L., Liu, X., Zhao, G., Ma, W., Qi, W., Ren, Z., Liao, H., Liu, M., Cai, D., Fang, H., 2020. Influence of the pore size and porosity of selective laser melted Ti6Al4V ELI porous scaffold on cell proliferation, osteogenesis and bone ingrowth. Mater. Sci. Eng. C 106, 110289. https://doi.org/10.1016/j.msec.2019.110289.

Costa, M.M., Bartolomeu, F., Alves, N., Silva, F.S., Miranda, G., 2019a. Tribological behavior of bioactive multi-material structures targeting orthopedic applications. J. Mech. Behav. Biomed. Mater. 94, 193–200. https://doi.org/10.1016/j.jmbbm.2019.02.028.

Costa, M.M., Bartolomeu, F., Palmeiro, J., Guimarães, B., Alves, N., Miranda, G., Silva, F. S., 2021. Multi-material NiTi-PEEK hybrid cellular structures by selective laser melting and hot pressing: tribological characterization. Tribol. Int. 156, 106830 https://doi.org/10.1016/j.triboint.2020.106830.

Costa, M.M., Dantas, T.A., Bartolomeu, F., Alves, N., Silva, F.S., Miranda, G., Toptan, F., 2019b. Corrosion behaviour of PEEK or β-TCP-impregnated Ti6Al4V SLM structures targeting biomedical applications. Trans. Nonferrous Metals Soc. China 29, 2523–2533. https://doi.org/10.1016/S1003-6326(19)65160-5.

Costa, M.M., Lima, R., Melo-Fonseca, F., Bartolomeu, F., Alves, N., Miranda, A., Gasik, M., Silva, F.S., Silva, N.A., Miranda, G., 2019c. Development of β-TCP-Ti6Al4V structures: driving cellular response by modulating physical and chemical properties. Mater. Sci. Eng. C 98, 705–716. https://doi.org/10.1016/j.msec.2019.01.016.

Dantas, T.A., Abreu, C.S., Costa, M.M., Miranda, G., Silva, F.S., Dourado, N., Gomes, J.R., 2017. Bioactive materials driven primary stability on titanium biocomposites. Mater. Sci. Eng. C 77, 1104–1110. https://doi.org/10.1016/j.msec.2017.04.014.

Dulski, M., Dudek, K., Grelowski, M., Kubacki, J., Hertlein, J., Wojtyniak, M., Goryczka, T., 2018. Impact of annealing on features of BCP coating on NiTi shape memory alloy: preparation and physicochemical characterization. Appl. Surf. Sci. 437, 28–40. https://doi.org/10.1016/j.apsusc.2017.12.056.

Faria, D., Abreu, C.S., Buciumeanu, M., Dourado, N., Carvalho, O., Silva, F.S., Miranda, G., 2018. Ti6Al4V laser surface preparation and functionalization using hydroxyapatite for biomedical applications. J. Biomed. Mater. Res. B Appl. Biomater. 106B, 1534–1545. https://doi.org/10.1002/jbm.b.33964.

Faria, D., Henriques, B., Souza, A.C., Silva, F.S., Carvalho, O., 2020. Laser-assisted production of HAp-coated zirconia structured surfaces for biomedical applications. J. Mech. Behav. Biomed. Mater. 112, 104049 https://doi.org/10.1016/j.jmbbm.2020.104049.

Gao, P., Fan, B., Yu, X., Liu, W., Wu, J., Shi, L., Yang, D., Tan, L., Wan, P., Hao, Y., Li, S., Hou, W., Yang, K., Li, X., Guo, Z., 2020. Biofunctional magnesium coated Ti6Al4V scaffold enhances osteogenesis and angiogenesis in vitro and in vivo for orthopedic application. Bioact. Mater. 5, 680–693. https://doi.org/10.1016/j.bioactmat.2020.04.019.

Harb, S.V., Bassous, N.J., de Souza, T.A.C., Trentin, A., Pulcinelli, S.H., Santilli, C.V., Webster, T.J., Lobo, A.O., Hammer, P., 2020. Hydroxyapatite and β-TCP modified PMMA-TiO2 and PMMA-ZrO2 coatings for bioactive corrosion protection of Ti6Al4V implants. Mater. Sci. Eng. C 116, 111149. https://doi.org/10.1016/j.msec.2020.111149.

Hung, C.H., Chang, F.Y., Chang, T.L., Chang, Y.T., Huang, K.W., Liang, P.C., 2015. Micromachining NiTi tubes for use in medical devices by using a femtosecond laser. Opt Laser. Eng. 66, 34–40. https://doi.org/10.1016/j.optlaseng.2014.08.001.

Lei, P., Qian, H., Zhang, T., Lei, T., Hu, Y., Chen, C., Zhou, K., 2022. Porous tantalum structure integrated on Ti6Al4V base by Laser Powder Bed Fusion for enhanced bony-ingrowth implants: in vitro and in vivo validation. Bioact. Mater. 7, 3–13. https://doi.org/10.1016/j.bioactmat.2021.05.025.

Liu, Y., Wang, G., Cai, Y., Ji, H., Zhou, G., Zhao, X., Tang, R., Zhang, M., 2009. In vitro effects of nanophase hydroxyapatite particles on proliferation and osteogenic differentiation of bone marrow-derived mesenchymal stem cells. J. Biomed. Mater. Res. 90, 1083–1091. https://doi.org/10.1002/jbm.a.32192.

MacBarb, R.F., Lindsey, D.P., Bahney, C.S., Woods, S.A., Wolfe, M.L., Yerby, S.A., 2017. Fortifying the bone-implant interface part 1: an in vitro evaluation of 3D-printed and TPS porous surfaces. Int. J. Spine Surg. 11, 105–115. https://doi.org/10.14444/4015.

Madeira, S., Barbosa, A., Moura, C.G., Buciumeanu, M., Silva, F.S., Carvalho, O., 2020. Aunps and Agμps-functionalized zirconia surfaces by hybrid laser technology for dental implants. Ceram. Int. 46, 7109–7121. https://doi.org/10.1016/j.ceramint.2019.11.203.

Melo-Fonseca, F., Lima, R., Costa, M.M., Bartolomeu, F., Alves, N., Miranda, A., Gasik, M., Silva, F.S., Silva, N.A., Miranda, G., 2018. 45S5 BAG-Ti6Al4V structures: the influence of the design on some of the physical and chemical interactions that drive cellular response. Mater. Des. 160, 95–105. https://doi.org/10.1016/J.MATDES.2018.08.056.

Mitra, I., Bose, S., Dernell, W.S., Dasgupta, N., Eckstrand, C., Herrick, J., Yaszemski, M.J., Goodman, S.B., Bandyopadhyay, A., 2021. 3D Printing in alloy design to improve biocompatibility in metallic implants. Mater. Today 45, 20–34. https://doi.org/10.1016/j.mattod.2020.11.021.

Moura, C.G., Pereira, R., Buciumeanu, M., Carvalho, O., Bartolomeu, F., Nascimento, R., Silva, F.S., 2017. Effect of laser surface texturing on primary stability and surface properties of zirconia implants. Ceram. Int. 43, 15227–15236. https://doi.org/10.1016/j.ceramint.2017.08.058.

Müller, V., Balvay, S., Gaillard, C., Tadier, S., Gremillard, L., Djurado, E., 2021. One-step fabrication of single-phase hydroxyapatite coatings on Ti-alloy implants by electrostatic spray deposition: from microstructural investigation to in vitro studies. Surf. Coating. Technol. 427, 127805 https://doi.org/10.1016/j.surfcoat.2021.127805.

Mwangi, J.W., Nguyen, L.T., Bui, V.D., Berger, T., Zeidler, H., Schubert, A., 2019. Nitinol manufacturing and micromachining: a review of processes and their suitability in processing medical-grade nitinol. J. Manuf. Process. 38, 355–369. https://doi.org/10.1016/j.jmapro.2019.01.003.

Nakagawa, Y., Muneta, T., Tsuji, K., Ichinose, S., Hakamatsuka, Y., Koga, H., Sekiya, I., 2013. β-Tricalcium phosphate micron particles enhance calcification of human mesenchymal stem cells in vitro. J. Nanomater., 426786 https://doi.org/10.1155/2013/426786, 2013.

Park, J.S., Lee, S.J., Jo, H.H., Lee, J.H., Kim, W.D., Lee, J.Y., Park, S.A., 2017. Fabrication and characterization of 3D-printed bone-like β-tricalcium phosphate/polycaprolactone scaffolds for dental tissue engineering. J. Ind. Eng. Chem. 46, 175–181. https://doi.org/10.1016/j.jiec.2016.10.028.

Parvizi, S., Hashemi, S.M., Asgarinia, F., Nematollahi, M., Elahinia, M., 2021. Effective parameters on the final properties of NiTi-based alloys manufactured by powder metallurgy methods: a review. Prog. Mater. Sci. 117, 100739 https://doi.org/10.1016/j.pmatsci.2020.100739.

Peñarrieta-juanito, G., Cruz, M., Costa, M., Miranda, G., Marques, J., Magini, R., Mata, A., Souza, J.C.M., Caramês, J., Silva, F.S., 2018. A novel gradated zirconia implant material embedding bioactive ceramics: osteoblast behavior and physicochemical assessment. Materialia 1, 3–14. https://doi.org/10.1016/j.mtla.2018.07.002.

Peñarrieta-Juanito, G.M., Costa, M., Cruz, M., Miranda, G., Henriques, B., Marques, J., Magini, R., Mata, A., Caramês, J., Silva, F., Souza, J.C.M., 2018. Bioactivity of novel functionally structured titanium-ceramic composites in contact with human osteoblasts. J. Biomed. Mater. Res. 106, 1923–1931. https://doi.org/10.1002/jbm.a.36394.

Ran, Q., Yang, W., Hu, Y., Shen, X., Yu, Y., Xiang, Y., Cai, K., 2018. Osteogenesis of 3D printed porous Ti6Al4V implants with different pore sizes. J. Mech. Behav. Biomed. Mater. 84, 1–11. https://doi.org/10.1016/j.jmbbm.2018.04.010.

Reddy, B.N.K., Udayashankar, N.K., 2016. The effect of annealing temperature on the structural, morphological, mechanical and surface properties of intermetallic NiTi alloy thin films. Surface. Interfac. 5, 62–71. https://doi.org/10.1016/j.surfin.2016.09.007.

Ribeiro-Samy, S., Silva, N.A., Correlo, V.M., Fraga, J.S., Pinto, L., Teixeira-Castro, A., Leite-Almeida, H., Almeida, A., Gimble, J.M., Sousa, N., Salgado, A.J., Reis, R.L., 2013. Development and characterization of a PHB-HV-based 3D scaffold for a tissue engineering and cell-therapy combinatorial approach for spinal cord injury regeneration. Macromol. Biosci. 13, 1576–1592. https://doi.org/10.1002/mabi.201300178.

Sevcikova, J., Pavkova Goldbergova, M., 2017. Biocompatibility of NiTi alloys in the cell behaviour. Biometals 30, 163–169. https://doi.org/10.1007/s10534-017-0002-5.

Shekhawat, D., Singh, A., Patnaik, A., 2021. Tribo-behaviour of biomaterials for hip arthroplasty. Mater. Today Proc. 44, 4809–4815. https://doi.org/10.1016/j.matpr.2020.11.420.

Silva, N.A., Salgado, A.J., Sousa, R.A., Oliveira, J.T., Pedro, A.J., Leite-Almeida, H., Cerqueira, R., Almeida, A., Mastronardi, F., Mano, J.F., Neves, N.M., Sousa, N., Reis, R.L., 2010. Development and characterization of a novel hybrid tissue engineering–based scaffold for spinal cord injury repair. Tissue Eng. 16, 45–54. https://doi.org/10.1089/ten.tea.2008.0559.

Silva, R., Ferreira, H., Carvalho, A.C., Gomes, A.C., Cavaco-Paulo, A., 2012. Protein microspheres as suitable devices for piroxicam release. Colloids Surf. B Biointerfaces 92, 277–285. https://doi.org/10.1016/j.colsurfb.2011.11.050.

Solanke, S., Gaval, V., Sanghavi, S., 2021. In vitro tribological investigation and osseointegration assessment for metallic orthopedic bioimplant materials. Mater. Today Proc. 44, 4173–4178. https://doi.org/10.1016/j.matpr.2020.10.528.

Straumann, 2011. In: Scientific Evidence, first ed., pp. 1–36 2011.

Taniguchi, N., Fujibayashi, S., Takemoto, M., Sasaki, K., Otsuki, B., Nakamura, T., Matsushita, T., Kokubo, T., Matsuda, S., 2016. Effect of pore size on bone ingrowth into porous titanium implants fabricated by additive manufacturing: an in vivo experiment. Mater. Sci. Eng. C 59, 690–701. https://doi.org/10.1016/j.msec.2015.10.069.

Tiainen, L., Abreu, P., Buciumeanu, M., Silva, F., Gasik, M., Serna Guerrero, R., Carvalho, O., 2019. Novel laser surface texturing for improved primary stability of titanium implants. J. Mech. Behav. Biomed. Mater. 98, 26–39. https://doi.org/10.1016/j.jmbbm.2019.04.052.

Toptan, F., Alves, A.C., Carvalho, Ó., Bartolomeu, F., Pinto, A.M.P., Silva, F., Miranda, G., 2019. Corrosion and tribocorrosion behaviour of Ti6Al4V produced by selective laser melting and hot pressing in comparison with the commercial alloy. J. Mater. Process. Technol. 266, 239–245. https://doi.org/10.1016/j.jmatprotec.2018.11.008.

Verma, S., Sharma, N., Kango, S., Sharma, S., 2021. Developments of PEEK (Polyetheretherketone) as a biomedical material: a focused review. Eur. Polym. J. 147, 110295 https://doi.org/10.1016/j.eurpolymj.2021.110295.

Wedemeyer, C., Jablonski, H., Mumdzic-Zverotic, A., Fietzek, H., Mertens, T., Hilken, G., Krüger, C., Wissmann, A., Heep, H., Schlepper, R., Kauther, M.D., 2019. Laser-induced nanostructures on titanium surfaces ensure osseointegration of implants in rabbit femora. Materialia 6, 100266. https://doi.org/10.1016/j.mtla.2019.100266.

Westhrin, M., Xie, M., Olderøy, M., Sikorski, P., Strand, B.L., Standal, T., 2015. Osteogenic differentiation of human mesenchymal stem cells in mineralized alginate matrices. PLoS One 10, e0120374. https://doi.org/10.1371/journal.pone.0120374.

Wittenberg, R.H., Steffen, R., Windhagen, H., Bücking, P., Wilcke, A., 2013. Five-year results of a cementless short-hip-stem prosthesis. Orthop. Rev. 5, 16–22. https://doi.org/10.4081/or.2013.e4.

Yang, F., Chen, C., Zhou, Q., Gong, Y., Li, R., Li, C., Klämpfl, F., Freund, S., Wu, X., Sun, Y., Li, X., Schmidt, M., Ma, D., Yu, Y., 2017. Laser beam melting 3D printing of Ti6Al4V based porous structured dental implants: fabrication, biocompatibility analysis and photoelastic study. Sci. Rep. 7, 45360. https://doi.org/10.1038/srep45360.

Yuan, L., Ding, S., Wen, C., 2019. Additive manufacturing technology for porous metal implant applications and triple minimal surface structures: a review. Bioact. Mater. 4, 56–70. https://doi.org/10.1016/j.bioactmat.2018.12.003.

Zheng, J., Zhao, H., Dong, E., Kang, J., Liu, C., Sun, C., Li, D., Wang, L., 2021. Additively-manufactured PEEK/HA porous scaffolds with highly-controllable mechanical properties and excellent biocompatibility. Mater. Sci. Eng. C 128, 112333. https://doi.org/10.1016/j.msec.2021.112333.